

ACCEPTED MANUSCRIPT • OPEN ACCESS

## Atlas construction and spatial normalisation to facilitate radiation-induced late effects research in childhood cancer

To cite this article before publication: Catarina Veiga *et al* 2021 *Phys. Med. Biol.* in press <https://doi.org/10.1088/1361-6560/abf010>

### Manuscript version: Accepted Manuscript

Accepted Manuscript is “the version of the article accepted for publication including all changes made as a result of the peer review process, and which may also include the addition to the article by IOP Publishing of a header, an article ID, a cover sheet and/or an ‘Accepted Manuscript’ watermark, but excluding any other editing, typesetting or other changes made by IOP Publishing and/or its licensors”

This Accepted Manuscript is © 2021 Institute of Physics and Engineering in Medicine.

As the Version of Record of this article is going to be / has been published on a gold open access basis under a CC BY 3.0 licence, this Accepted Manuscript is available for reuse under a CC BY 3.0 licence immediately.

Everyone is permitted to use all or part of the original content in this article, provided that they adhere to all the terms of the licence <https://creativecommons.org/licenses/by/3.0>

Although reasonable endeavours have been taken to obtain all necessary permissions from third parties to include their copyrighted content within this article, their full citation and copyright line may not be present in this Accepted Manuscript version. Before using any content from this article, please refer to the Version of Record on IOPscience once published for full citation and copyright details, as permissions may be required. All third party content is fully copyright protected and is not published on a gold open access basis under a CC BY licence, unless that is specifically stated in the figure caption in the Version of Record.

View the [article online](#) for updates and enhancements.

## TITLE PAGE

## TITLE

Atlas construction and spatial normalisation to facilitate radiation-induced late effects research in childhood cancer

## AUTHOR LIST

Dr Catarina Veiga, [c.veiga@ucl.ac.uk](mailto:c.veiga@ucl.ac.uk), Centre for Medical Image Computing, Department of Medical Physics and Biomedical Engineering, University College London, London, UK; ORCID: 0000-0002-4132-2554

Dr Pei Lim, [pei.lim@nhs.net](mailto:pei.lim@nhs.net), Department of Oncology, University College London Hospital NHS Trust, London, UK; ORCID: 0000-0001-9633-7908

Ms Virginia Marin Anaya, [virginia.marinanaya1@nhs.net](mailto:virginia.marinanaya1@nhs.net), Radiotherapy Physics Services, University College London Hospital NHS Trust, London, UK; ORCID: 0000-0001-7844-7759

Dr Edward Chandy, [e.chandy@ucl.ac.uk](mailto:e.chandy@ucl.ac.uk), UCL Cancer Institute, University College London, London, UK; ORCID: 0000-0002-6117-8692

Dr Reem Ahmad, [r.h.ahmad@ucl.ac.uk](mailto:r.h.ahmad@ucl.ac.uk), Centre for Medical Image Computing, Department of Medical Physics and Biomedical Engineering, University College London, London, UK; ORCID: 0000-0001-5529-9802

Mr Derek D'Souza, [derek.dsouza@nhs.net](mailto:derek.dsouza@nhs.net), Radiotherapy Physics Services, University College London Hospital NHS Trust, London, UK; ORCID:0000-0002-4393-7683

Dr Mark Gaze, [mgaze@nhs.net](mailto:mgaze@nhs.net), Department of Oncology, University College London Hospital NHS Trust, London, UK; ORCID: 0000-0002-8344-7902

Mr Syed Moinuddin, [syed.moinuddin@nhs.net](mailto:syed.moinuddin@nhs.net), Radiotherapy, University College London Hospital NHS Trust, London, UK; ORCID:

1  
2  
3 Dr Jennifer Gains, [jenny.gains@nhs.net](mailto:jenny.gains@nhs.net), Department of Oncology, University College  
4 London Hospital NHS Trust, London, UK; ORCID:  
5  
6  
7

## 8 **KEY WORDS**

9

10  
11 childhood cancer, computed tomography, radiotherapy, image registration, spatial  
12 normalisation, anatomical atlas  
13  
14  
15

## 16 **ACKNOWLEDGMENTS**

17

18  
19 We wish to thank Mairead Daly (University College London Hospital) for data collation and  
20 Dr Jamie McClelland (University College London) for insightful discussions on the  
21 manuscript. VMA would like to express thanks to the whole Radiotherapy Physics  
22 department (both photon and proton physics groups) at University College London Hospital  
23 for their contributions to photon and proton treatment plans. CV is supported by the Royal  
24 Academy of Engineering under the Research Fellowship scheme (RF\201718\17140). RA  
25 was supported by National Institute for Health Research University College London  
26 Hospitals Biomedical Research Centre and Wellcome Trust Institutional Strategic Support  
27 Fund (WISSF). Dr M. N. Gaze is supported by the National Institute for Health Research  
28 Biomedical Research Centre of University College London Hospitals and by the Radiation  
29 Research Unit at the Cancer Research UK City of London Centre Award [C7893/A28990].  
30  
31  
32  
33  
34  
35  
36  
37  
38  
39  
40  
41  
42  
43  
44  
45  
46  
47  
48  
49  
50  
51  
52  
53  
54  
55  
56  
57  
58  
59  
60

**ABSTRACT**

Reducing radiation-induced side effects is one of the most important challenges in paediatric cancer treatment. Recently, there has been growing interest in using spatial normalisation to enable voxel-based analysis of radiation-induced toxicities in a variety of patient groups. The need to consider three-dimensional distribution of doses, rather than dose-volume histograms, is desirable but not yet explored in paediatric populations. In this paper, we investigate the feasibility of atlas construction and spatial normalisation in paediatric radiotherapy. We used planning computed tomography (CT) scans from twenty paediatric patients historically treated with craniospinal irradiation to generate a template CT that is suitable for spatial normalisation. This childhood cancer population representative template was constructed using groupwise image registration. An independent set of 53 subjects from a variety of childhood malignancies was then used to assess the quality of the propagation of new subjects to this common reference space using deformable image registration (i.e., spatial normalisation). The method was evaluated in terms of overall image similarity metrics, contour similarity and preservation of dose-volume properties. After spatial normalisation, we report a dice similarity coefficient of  $0.95 \pm 0.05$ ,  $0.85 \pm 0.04$ ,  $0.96 \pm 0.01$ ,  $0.91 \pm 0.03$ ,  $0.83 \pm 0.06$  and  $0.65 \pm 0.16$  for brain and spinal canal, ocular globes, lungs, liver, kidneys and bladder. We then demonstrated the potential advantages of an atlas-based approach to study the risk of second malignant neoplasms after radiotherapy. Our findings indicate satisfactory mapping between a heterogeneous group of patients and the template CT. The poorest performance was for organs in the abdominal and pelvic region, likely due to respiratory and physiological motion and to the highly deformable nature of abdominal organs. More specialised algorithms should be explored in the future to improve mapping in these regions. This study is the first step toward voxel-based analysis in radiation-induced toxicities following paediatric radiotherapy.

30

## MAIN BODY

## 1. INTRODUCTION

Radiation therapy (RT) is currently used to treat 40 to 50% of childhood cancer cases in the UK (The Royal College of Radiologists 2019). While the radiation is precisely targeted to destroy the cancer cells, it may also damage surrounding healthy cells leading to sequelae that can appear years to decades after treatment (Arain *et al*/2015). The higher risk of radiation-induced late effects in children is linked to the increased sensitivity of developing tissues, where radiation induces both organ damage and impairment of maturational processes (Paulino *et al* 2010). Furthermore, with current survival rates reaching 75% at 10-years (Cancer Research UK 2015), most paediatric patients become long term survivors allowing for late effects to manifest. The long term harmful effects of radiotherapy include infertility, impaired physical growth and pubertal development (Schwartz 1999), renal problems (Skinner 2018), neurocognitive deficits (Roddy and Mueller 2016), as well as a range of other life-threatening issues. Second cancers are the leading cause of mortality in long term survivors, followed by cardiac and pulmonary death (Armstrong *et al* 2009). Reducing radiation-induced side effects is one of the most important ongoing challenges in paediatric cancer treatment, but there is a lack of evidence-based dose/volume guidelines to inform treatment planning. This has recently been recognised internationally with the establishment of the Paediatric Normal Tissue Effects in the Clinic (PENTEC) task force (Constine *et al* 2019), which seeks to increase knowledge about paediatric radiotherapy dose constraints using published data.

Mathematical models of radiation-induced side effects are a powerful tool to guide treatment planning and clinical decision-making. The development and validation of treatment toxicity models is however very challenging, and when considering paediatric populations specific obstacles must be addressed (Constine *et al*/2019). Radiation dose to volume is the key predictive factor of radiation-induced effects. In adults, radiation-induced effects occur mostly in organs within the radiotherapy target volumes. In contrast, for children organs and tissues outside the target volume are also important, as side-effects may develop in different regions receiving lower doses at different timescales. It is common for treatments to encompass large volumes in comparison to children's body size (e.g, in craniospinal irradiation), meaning a wider range of organs and tissues can receive a significant radiation dose. Smaller bodies also cause organs to be closer to the high-dose regions, increasing dose due to secondary radiation. Tissues and organs which are not directly irradiated may still have a long-term risk of radiation-induced second cancers, as result of leakage and scattered radiation (Xu *et al*/2008, Harrison 2013). Additionally, the quality of toxicity models depends on the quantity and quality of the data. Collating large

1  
2  
3 datasets for individual cancer types is challenging as childhood cancers are both rare and  
4 heterogeneous (Pappo *et al*/2015). Moreover, routine clinical data is not detailed and has  
5  
6 70 limited delineations of organs and tissues; likewise, anatomy remote from the target  
7 volume is not usually imaged. To achieve larger sample sizes, it is desirable to identify  
8 methodologies that can leverage all clinically existing anatomical and dosimetric  
9 information from this heterogeneous cohort, including partial data. This can potentially be  
10 achieved by finding solutions to group patients according to organ at risk and not disease  
11  
12 75 diagnosis (Constine *et al*/2019). Radiotherapy delivery is rapidly evolving, with advanced  
13 techniques such as intensity modulated radiotherapy, intensity modulated arc-therapy  
14 (IMAT), helical tomotherapy, passive scattering proton therapy, and pencil beam scanning  
15 proton therapy (PBS-PT) becoming more accessible (Sterzing *et al*/2009, Mesbah *et al*/  
16 2011, Ludmir *et al*/2018, Padovani *et al*/2019). These not only change the characteristics  
17  
18 80 of dose distribution in healthy tissues (for example, low dose bath in IMAT and biological  
19 effectiveness of protons), but also make it even more challenging to achieve larger sample  
20 sizes for assessment per modality.  
21  
22  
23  
24

25 To address these challenges and facilitate analysis of complex 3D imaging and  
26 treatment data from heterogeneous patient groups, a possible solution to is to define a 3D  
27  
28 85 common reference space and normalise spatial information from individuals of the patient  
29 group into it. Image registration is used to propagate spatial data (such as 3D imaging  
30 information and dosimetry) from the individuals onto the common reference space, which  
31 may be defined as a representative subject or unbiased population atlases (Joshi *et al*/  
32 2004, Ghosh *et al*/2010). Spatial normalisation allows one to move from region-of-interest  
33  
34 90 to voxel-based analysis, which is particularly desirable in radiotherapy research to  
35 understand dose-toxicity relationships (Palma *et al*/2020). Spatial normalisation preserves  
36 the 3D information of the dose distributions (Monti *et al*/2018), unlike traditional techniques  
37 that simplify volumetric dose into 2D dose-volume histograms (DVHs). It is an  
38 advantageous approach that allows one to identify heterogeneous regional radiosensitivity  
39  
40 95 (i.e. sub-volumes of organs and tissues) while not relying on *a priori* definition of volumes  
41 (Palma *et al*/2020). The need to consider the actual spatial distribution of doses, rather  
42 than organ DVHs, is recognised in late normal tissue damage research for paediatric  
43 populations (Trott 2017). Spatial normalisation in radiotherapy has become a topic of  
44 interest in recent years, with recent studies focusing on radiation-induced side-effects on  
45 prostate, head and neck and lung (Acosta *et al*/2013, Palma *et al*/2016, Dréan *et al*/2016,  
46 Monti *et al*/2017, Beasley *et al*/2018, Mylona *et al*/2019, Marcello *et al*/2020, Mylona *et al*/  
47 2020, McWilliam *et al*/2020) and to predict outcomes (Ibragimov *et al*/2019).  
48  
49  
50  
51  
52  
53

54 In this work, we investigate the feasibility of atlas construction and spatial  
55 normalisation in paediatric radiotherapy to enable voxel-based analysis of radiation-  
56  
57 105 induced toxicities. The methodology was developed to serve as a framework to facilitate  
58 the development, validation, and clinical translation of radiotherapy-induced late effects  
59  
60

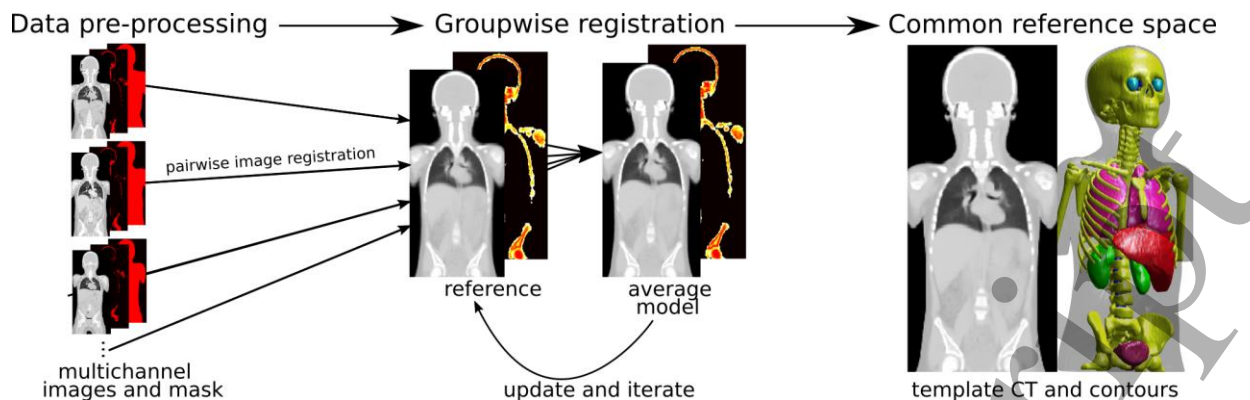
1  
2  
3 models in childhood cancer patients. The atlas-based approach allows one to spatially  
4 standardise a heterogenous population in an unbiased way, while preserving localised  
5 spatial anatomical, functional and dosimetric information.  
6  
7

110

## 11 2. METHODS AND MATERIALS

### 13 2.1. Paediatric atlas construction

17 115 To spatially normalise complex anatomical and treatment imaging data, image  
18 registration is used to propagate information from individual subjects onto a common  
19 reference space. The first key step is to define a reference space representative of the  
20 population being studied. For our application, a simple, common, popular and scalable  
21 approach is to choose as reference space the planning computed tomography (CT) scan of  
22 a representative subject from the population (e.g., subject with average age or average  
23 height). However, the selection of a single subject as reference space introduces bias to  
24 120 the registrations which propagates to subsequent analysis. For example, if the selected  
25 reference volume has atypical anatomical features then all registrations are potentially  
26 more challenging and will estimate atypical and/or implausible transformations  
27 (Namburete *et al* 2018). Choosing an adequate reference is a challenging problem,  
28 particularly for the paediatric cancer population, known to be heterogeneous and prone  
29 to deviations in anatomy. Anatomical variations can occur simply due to changes with  
30 age, but more complex variations can occur with the treatments used, increasing the risk  
31 of individual subjects having atypical features. For example, some require invasive  
32 125 therapies which may cause co-morbidities and require additional interventions that are  
33 visible on CT imaging (such as the use of shunts or changed anatomy from surgical  
34 interventions). For such reasons, we opted to construct the reference space using  
35 groupwise image registration and paediatric radiotherapy CT images. Groupwise image  
36 registration is a process that iteratively alternates between co-registration of all subjects  
37 to a reference image and updating this reference image with the average model produced.  
38 130 Figure 1 provides a schematic overview of the pipeline proposed, which is detailed in the  
39 following sections.  
40  
41  
42  
43  
44  
45  
46  
47  
48  
49  
50  
51  
52  
53  
54  
55  
56  
57  
58  
59  
60



140 *Figure 1- Schematic of pipeline used to generate the paediatric common reference space.*  
 141 *The pipeline is divided into three main steps: (1) Data pre-processing: definition of inputs*  
 142 *to be used in pairwise registrations (multichannel images and corresponding masks); (2)*  
 143 *Groupwise image registration: iterative process of registering a set of images together to*  
 144 *a common reference space; (3) Atlas construction: generate template CT and contours.*

145

### 2.1.1 Patient data

146 The paediatric radiotherapy data used in our study was requested in line with the  
 147 internal information governance procedures of the University College London Hospital  
 148 (UCLH) Radiotherapy Department and was provided as fully-anonymised datasets. For  
 149 atlas construction we used data from twenty children historically treated with 3D conformal  
 150 photon craniospinal irradiation (CSI). This included 10 boys and 10 girls with a median age  
 151 of 8 y (range: 3 - 15 y). All patients underwent a CT scan of the brain and whole spine,  
 152 immobilised in the treatment position, for radiotherapy planning purposes. For simplicity,  
 153 CSI CT scans are labelled as whole-body (as all major organs are visible), but limbs are  
 154 usually partially out-of-field. Imaging resolution for all scans was  $0.98 \times 0.98 \times 2.5 \text{ mm}^3$ . The  
 155 following RT structures were used for validation purposes in the study: central nervous  
 156 system (CNS) (whole brain and spinal canal down to L3), ocular globes, lungs, liver, kidneys  
 157 and bladder. This set of contours was chosen to be clinically relevant and to cover different  
 158 regions of the body. Clinically available contours were used if possible, and missing  
 159 contours were additionally generated. Hence, the segmentation dataset had inter-user  
 160 variability. All new contours were reviewed to clinically acceptable standards by an  
 161 oncologist (EC) and/or physicist (CV). Manual segmentation and review was performed  
 162 using the open-source software ITK-SNAP (Yushkevich *et al*/2006). Simple post-processing  
 163 was employed before analysis to all contours to remove common segmentation errors (e.g.  
 164 remove holes and discard small regions outside organ).

### 2.1.2. Pre-processing

1  
2  
3 170 The following pre-processing steps were applied to all CTs prior to atlas construction  
4 to generate the inputs for image registration. The CTs were corrected to exclude external  
5 elements (e.g., couch and anaesthesia equipment) and to ignore shunts and high-intensity  
6 artefacts. External elements were defined as voxels outside the body contour and were  
7 overwritten as air ( $HU=-1000$ ). High-intensity artefacts were replaced with “NaN” value so  
8 that they would not contribute to the average image constructed at each iteration.  
9  
10 175 Furthermore, since the location and volume of bowel gas is variable between patients and  
11 hence there is no true one-to-one mapping, bowel gas regions (defined from the body,  
12 inferior to the lungs, as  $HU<-200$ ) were overwritten with water intensity ( $HU=0$ ). A binary  
13 mask was defined as a dilation of the body contour and used as input to speed the  
14 registrations.  
15  
16 180

17  
18  
19 Inter-subject image registration is particularly challenging in the CSI paediatric  
20 population due to the heterogeneous anatomy of children of both sexes aged 2-16 years.  
21 To guide the deformable registrations between subjects with different body sizes, the input  
22 images were defined as multichannel images. The first channel corresponds to the pre-  
23 processed CT image, while the second channel corresponds to the binary mask of the  
24 individual’s skeleton (defined as  $HU>150$ ). All multichannel CTs (and respective masks)  
25 185 were also automatically cropped in the anterior-posterior direction to further reduce  
26 computation time and memory requirements.  
27  
28  
29

30  
31 The binary images used in the pre-processing were generated semi-automatically  
32 based on thresholding of the CTs, morphological operations and existing manual RT  
33 190 segmentations, and then visually inspected and manually corrected (if needed) to remove  
34 gross labelling errors.  
35  
36  
37  
38

### 39 ***2.1.3. Groupwise image registration***

40  
41 195 We constructed a reference space representative of the paediatric radiotherapy  
42 population using groupwise image registration. The output of interest is the final average  
43 intensity image produced, which we denominate as the “template CT” from here onwards.  
44 We have modified the method available in NiftyReg ([https://github.com/KCL-](https://github.com/KCL-BMEIS/niftyreg)  
45 [BMEIS/niftyreg](https://github.com/KCL-BMEIS/niftyreg)) for groupwise registration, tailoring it for co-registration of whole-body CT  
46 images of paediatric subjects. The process is initialised by automatically selecting the  
47 initial reference to be the subject with closest age to the average age of the population  
48 200 studied. The pipeline then alternates between pairwise registration of all images to the  
49 reference image and updating the reference image at the end of each iteration. The  
50 updated reference is obtained by averaging the intensities of all the pairwise registration  
51 results whilst enforcing the mean of all transformations to be the identity transform. The  
52 complexity of the transformation model increases with iteration number, from rigid to fine  
53 deformable image registration (DIR). Coarser registrations allow one to initially capture the  
54  
55 205  
56  
57  
58  
59  
60

1  
2  
3 large global variations in subject height and weight, which are followed by finer  
4 210 registrations to capture the smaller intra-patient variations in organ shape and size. This  
5 refinement process hence facilitates the co-registration of subjects with different body  
6 sizes and reduces computation times. A total of eleven iterations (one rigid-only, two affine  
7 and eight deformable) was empirically defined as further iterations were found to not  
8 provide sharper mean images.  
9

10  
11  
12 215 Rigid and affine iterations use the block matching-based algorithm available in  
13 NiftyReg (Ourselin *et al* 2001, Modat *et al* 2014). Multichannel and cropped images were  
14 generated at the end of the last affine step and used in the following iterations. The DIR  
15 steps make use of the velocity fields parametrisation of the B-spline free form deformation  
16 based algorithm (Rueckert *et al* 1999, Modat *et al* 2012), guaranteeing transformations  
17 that are diffeomorphic, symmetric and inverse-consistent. All pairwise deformable  
18 220 registrations use a multi-resolution approach with five levels. Locally Normalised Cross  
19 Correlation (LNCC) and Sum Squared Difference (SSD) were used as similarity metrics in  
20 the CT and skeleton channels, respectively. Bending energy and linear elasticity penalty  
21 terms were used for regularisation in all registrations to encourage smooth deformations.  
22 The number of levels to perform and control point spacing were updated with iteration  
23 225 number to progressively recover finer deformations. The finest registrations were carried  
24 out using five resolution levels and a control grid spacing of 12.5 mm.  
25  
26

27  
28 In addition to generating the average CT image, at the last iteration the  
29 corresponding average contours are also generated by propagating and averaging the  
30 organ contours for all subjects (majority voting), using the same transformations.  
31 230  
32  
33

## 34 230 35 36 37 38 **2.2. Evaluation experiments**

39  
40  
41 To evaluate the constructed paediatric atlas for spatial normalisation, an  
42 235 independent set of 53 patients historically treated at UCLH was used. This evaluation  
43 dataset included 31 boys and 22 girls with a median age of 5 y (range: 1 - 16 y) from a  
44 variety of disease cohorts, including CSI (n=30), abdominal neuroblastomas (n=18), brain  
45 tumours (n=3) and Ewing sarcomas (n=2). Similarly to the data described in Section 2.1.1  
46 Patient data, planning CT images and corresponding contours (CNS, ocular globes, lungs,  
47 240 liver, kidneys and bladder) were used for analysis. Clinical RT doses were also available for  
48 every subject, with prescription and fractionation varying between patients. All subjects  
49 were registered to the template CT using affine followed by non-rigid registration. The  
50 registration parameters and pre-processing strategy were similar to those used for the  
51 finest pairwise registrations in the groupwise pipeline.  
52  
53  
54  
55  
56

57 245  
58  
59  
60

The quality of the spatial normalisation process was evaluated considering how well the registrations aligned organs at the common reference space and if dose-volume properties are preserved after registration; furthermore, smooth deformations are important to promote the preservation of dose-volume characteristics. To evaluate the mapping in regions without manual labels, intensity-based similarity and deformation metrics were calculated. All metrics of image quality, contour similarity and dose-volume characteristics used are defined in Table 1 and briefly described in the following paragraphs. The following nomenclature is used to differentiate the different spaces where three-dimensional subject-specific information (i.e. CT, contours and dose) are defined:  $s$  = information of each subject in its native coordinate system;  $t$  = information of the template CT itself on its own coordinate system (common reference space);  $s \rightarrow t$  = information propagated from the subject space into the template CT coordinate system via image registration.

Table 1- Quantities used in the evaluation of the spatial normalisation.

Quantity	Equation	Description
Normalised Cross-Correlation (NCC)	$NCC = \frac{\sum[(I_{s \rightarrow t}(r) - \bar{I}_{s \rightarrow t}) \times (I_t(r) - \bar{I}_t)]}{\sqrt{\sum(I_{s \rightarrow t}(r) - \bar{I}_{s \rightarrow t})^2 \times \sum(I_t(r) - \bar{I}_t)^2}}$	$I_A(r)$ is the pixel intensities (HU) in image A at voxel $r$ , and $\bar{I}_A$ the mean intensity. NCC is a metric of the degree of similarity between images. Ranges from -1 to 1 with highest values representing higher image similarity.
Root Mean Squared of intensity differences ( $HU_{RMS}$ )	$\Delta HU_{RMS} = \sqrt{\frac{1}{n} \sum (I_{s \rightarrow t}(r) - I_t(r))^2}$	$I_A$ are the pixel intensities (HU) in image A. $\Delta HU_{RMS}$ provides a measure of disparity in image intensities. Units of $\Delta HU_{RMS}$ : HU.
Average absolute local volume change ( $LVC_{avg}$ )	$LVC_{avg} = \frac{1}{n} \sum  LVC(r) ,$ where $LVC(r) = \begin{cases} 1 - 1/J(r) & J(r) < 1 \\ J(r) - 1 & J(r) \geq 1 \end{cases}$	LVC is the local volume change, computed from the determinant of the Jacobian ( $J$ ) of the deformation (Pilia et al 2019).
Dice Similarity Coefficient (DSC)	$DSC = 2 \times \frac{V_t \cap V_{s \rightarrow t}}{ V_t  +  V_{s \rightarrow t} }$	$V_A$ represents the voxels that define a volume of interest A. Ranges from 0 to 1, with highest values representing better contour overlap.

Jaccard Coefficient (JC)	$JC = \frac{V_t \cap V_{s \rightarrow t}}{V_t \cup V_{s \rightarrow t}}$	Ranges from 0 to 1, with highest values representing better contour overlap.
Average distance between surfaces ( $DT_{avg}$ )	$DT_{avg} = \max \{ \overline{DT_{s,s \rightarrow t}}, \overline{DT_{s \rightarrow t,s}} \}$	$\overline{DT_{A,B}}$ is the mean of the distribution of values for distance between each point on the surface of volume A to the closest point on the surface of volume B. Units of $DT_{avg}$ : mm.
Distance between centroids ( $\Delta TR$ )	$\Delta TR = \ R_{s \rightarrow t} - R_t\ $	$R_A$ is the centroid of a volume A. Units of $\Delta TR$ : mm.
Relative difference of areas of DVHs (RDA)	$RDA = \frac{\int  DVH_{s \rightarrow t} - DVH_s  dx}{\max \{ \int DVH_s dx, \int DVH_{s \rightarrow t} dx \}}$	$DVH_A$ is dose-volume histogram for volume A. RDA ranges from 0 and 1, with the lowest representing better DVH preservation. (Adapted from Acosta et al 2013).
Dose-organ overlap (DOO)	$DOO = \frac{\int_{V_t \cap V_{s \rightarrow t}} D_{s \rightarrow t}(x) dx}{\int_{V_t \cup V_{s \rightarrow t}} D_{s \rightarrow t}(x) dx}$	$V_A$ represents the voxels that define a volume of interest A, and $D_A$ the three-dimensional dose matrix inside A. DOO ranges from 0 and 1, with the highest values representing better DVH preservation (Acosta et al 2013).
<p>Definitions:</p> <ul style="list-style-type: none"> <li>• <math>s</math> = information of each subject in its native coordinate system;</li> <li>• <math>t</math> = information of the template CT itself on its own coordinate system (common reference space);</li> <li>• <math>s \rightarrow t</math> = information propagated from the subject space into the template CT coordinate system.</li> </ul>		

Intensity-based similarity was assessed by calculating the Normalised Cross Correlation (NCC) and the root mean square error ( $HU_{RMS}$ ) between the deformed CTs and template CT. To demonstrate the range of deformations recovered, we also computed the average absolute local volume change ( $LVC_{avg}$ ) using the determinant of the Jacobian of the pairwise deformations (Pilia *et al* 2019).

1  
2  
3 To describe the similarity between contours defined in the template space ( $V_t$ ) and  
4 the equivalent contours propagated from each subject to this space via image registration  
5 ( $V_{s \rightarrow t}$ ), we computed the Dice Similarity Coefficient (DSC), Jaccard Coefficient (JC), average  
6 distance between surfaces ( $DT_{avg}$ ) (Mishchenko 2015) and distance between centroids  
7 ( $\Delta TR$ ). These quantities measure accuracy of the registrations in mapping organ volume,  
8 location and shape.

9  
10  
11  
12 Spatial normalisation should preserve the dose-volume properties of each  
13 individual subject, such that DVH-based models of side-effects would be similar if  
14 performed on the subject or common reference space. The differences in the dose-volume  
15 histograms computed in the subject ( $DVH_s$ ) and template ( $DVH_{s \rightarrow t}$ ) spaces were assessed  
16 using the dose relative difference of areas of DVHs (RDA) and dose-organ overlap (D00)  
17 (Acosta *et al*/2013).  
18  
19  
20

21  
22 It should be noted that not all patients included had planning CTs that covered the  
23 same field-of-view, which may impact in the metrics reported. When computing different  
24 measures of registration quality, pixels outside the body and the common field-of-view  
25 were excluded from analysis.  
26  
27  
28

### 29 **2.3 Critical evaluation of spatial normalisation for radiation-induced second malignant** 30 **neoplasms risk**

31  
32  
33  
34 Our aim in this part of the study was to demonstrate the potential of the proposed  
35 atlas-based approach to facilitate radiation-induced late effects research in childhood  
36 cancer treatment (Figure 2). The risks of radiation-induced second malignant neoplasms  
37 (SMNs) were estimated for a group of patients using the common reference space ( $s \rightarrow t$ )  
38 and compared the equivalent values using the original subject space ( $s$ ). For this purpose,  
39 we used a subset of subjects for whom clinically acceptable dual radiotherapy plans were  
40 available. This included fourteen patients from different disease cohorts (from the  $n=53$   
41 evaluation cohort): CSI ( $n=3$ ), abdominal neuroblastomas ( $n=7$ ), brain tumours ( $n=3$ ) and  
42 Ewing's sarcoma ( $n=1$ ). A photon plan and a pencil-beam scanning proton therapy plan  
43 were available for risk estimation for each subject. As different patient groups and  
44 treatment modalities were included, this subgroup had variability in the 3D dose  
45 distributions considered. This was intentionally chosen such that organs were located in  
46 both homogeneous dose regions and within dose gradients, and with varying position  
47 relative to the RT field (i.e., inside the RT target, near-target and out-of-field). In the case  
48 of the proton therapy plans, an estimation of homogeneous whole body neutron dose was  
49 included (Schneider *et al*/2002). In addition to assessing mean and maximum organ doses  
50 ( $D_{avg}$  and  $D_{max}$ ), (i.e., linear dose-response model), a mechanistic model was used to  
51 estimate the excess absolute risk (EAR) of radiation-induced carcinomas in the CNS, lungs,  
52  
53  
54  
55  
56  
57  
58  
59  
60

liver, and bladder (Schneider *et al*/2011). This model accounts for cell killing, repopulation and fractionation effects and was developed for therapeutic exposures. EAR is estimated from the dose to volume data using the mechanistic dose-response model (i.e., non-linear model), and an age-dependent modifying function. Parameters depend on the tissues being irradiated, and are available in the original publication (Schneider *et al*/2011). We report the  $D_{avg}$ ,  $D_{max}$ , and EAR for both modalities, as well as the risk ratio (RR) between modalities. For convenience, the RR was defined to range between 0 and 1 such that it does not depend on which modality is estimated as superior:

$$RR = \min \left\{ \frac{EAR_{\text{protons}}}{EAR_{\text{photons}}}, \frac{EAR_{\text{photons}}}{EAR_{\text{protons}}} \right\}$$

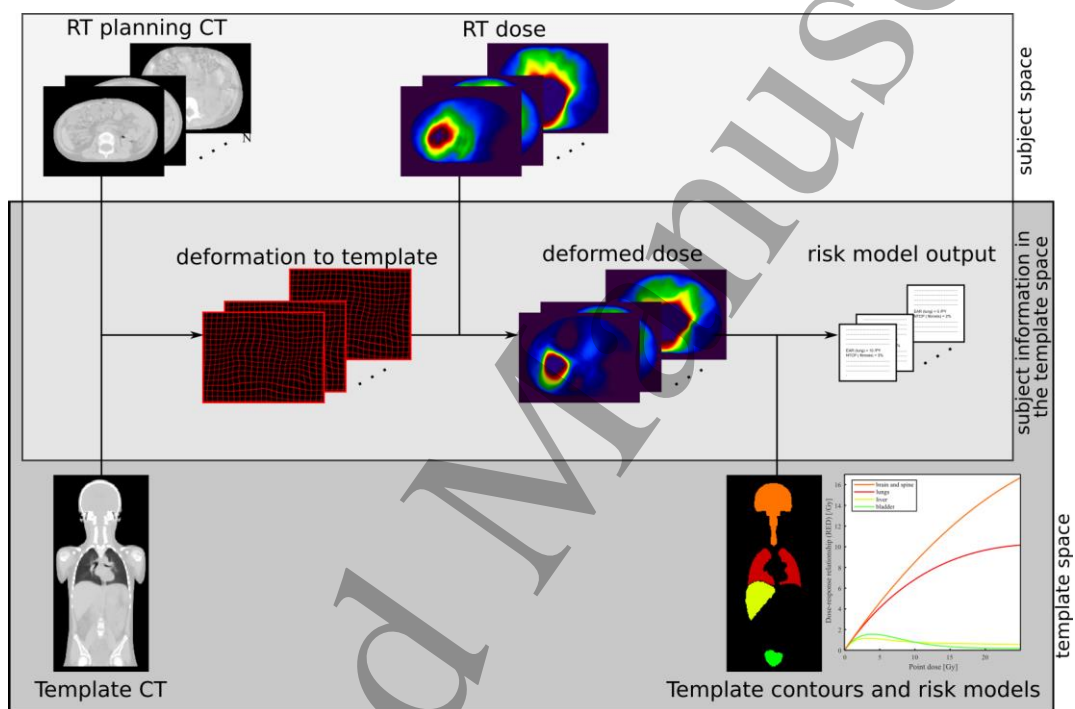


Figure 2- Diagram showing data workflow for spatial normalisation to facilitate radiation-induced late effects research.

## 2.4 Implementation details and data analysis

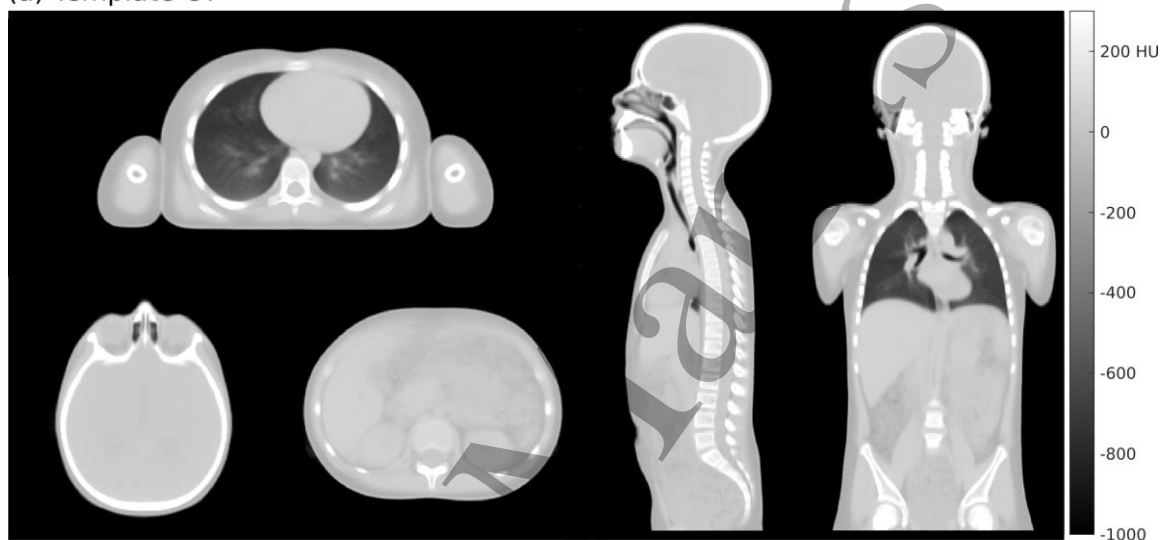
The pipelines for atlas construction, subject propagation, validation workflow and SMN models were implemented in Matlab 2019a (Mathworks Inc.). Statistical analysis was also performed in Matlab, using the Statistical Toolbox, with statistical significance set at 5%. Not every patient included had complete segmentation sets due to variations in the field-of-view covered by the planning CT. Therefore, the dimensions of the samples used were variable.

### 3. RESULTS

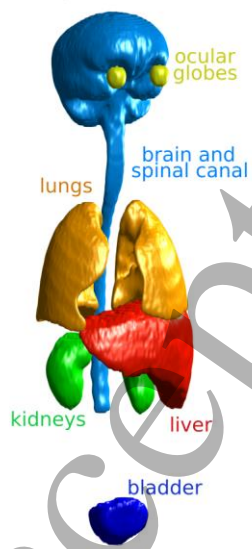
#### 3.1 Overview of the template space

The atlas construction took approximately  $35.5 \pm 0.5$  hours on a dual Intel® Xeon Gold 6134 CPU (3.20GHz), 128GB memory (computation was repeated three times). Figure 3 shows the atlas constructed using the twenty CSI subjects, as well as segmentations, average HU and volume differences per voxel. The deformable registration of all subjects to this template took  $66 \pm 30$  minutes (per subject) on the same system.

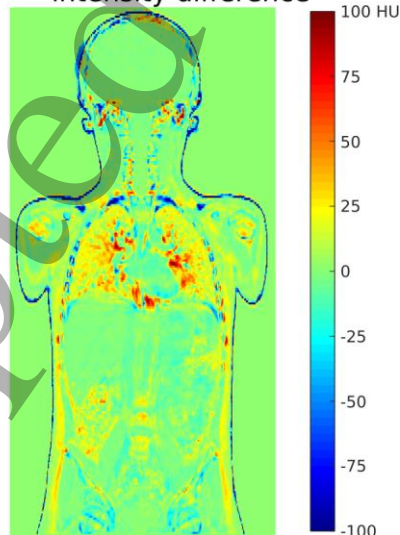
(a) Template CT



(b) Template contours



(c) Average local intensity difference



(d) Average local volume change

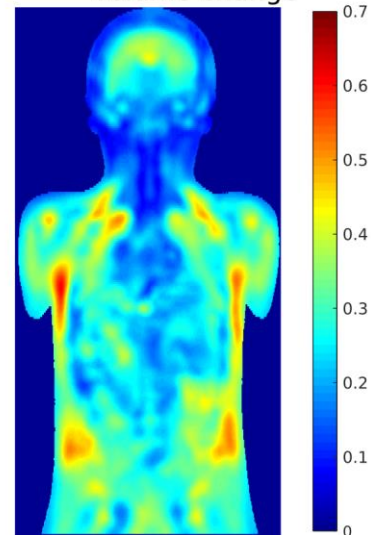
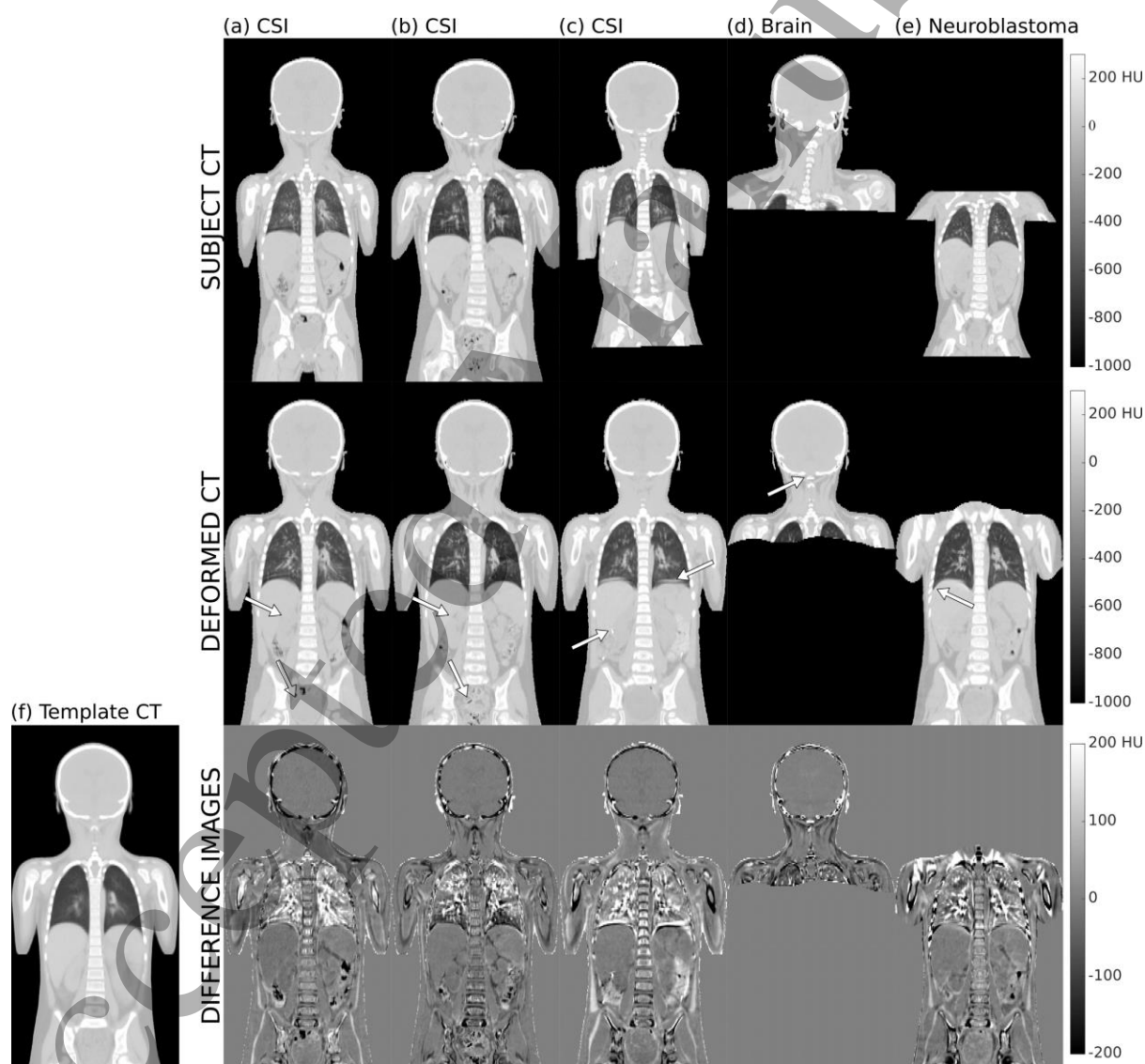


Figure 3- (a) Template CT generated using groupwise image registration on selected axial, sagittal and coronal views and (b) corresponding contours. (c) Map of local average intensity difference between template and subject CTs. (d) Map of average absolute value

of the local volume change when co-registering subjects. Maps resulted from averaging over the twenty subjects used for atlas construction, excluding pixels away from the body.

345 Figure 4 shows some examples of registrations for different disease cohorts, highlighting some of the common pitfalls of the spatial normalisation process. The registrations were able to successfully align the overall anatomy at the common reference space despite the wide variation in age, height, and weight between subjects. Large local deformations were challenging to completely capture, and visually we could identify common patterns of misregistration such as local misalignment of individual bones (e.g. individual vertebrae and ribs) and poor matching at soft tissue boundaries (e.g. between right kidney and liver). Image quality was an important source of registration variability contributing to fuzzier aspect in regions without consistently sharp anatomical boundaries.



355 Figure 4- Examples of registrations to the (f) template CT, including subjects from (a-c) craniospinal irradiation (CSI) and (d-e) other disease cohorts. Top row: subject CT scans

1  
2  
3  
4  
5  
6 360  
7  
8  
9  
10  
11  
12  
13 365  
14  
15  
16  
17  
18  
19  
20  
21 370  
22  
23  
24  
25  
26  
27  
28  
29  
30  
31  
32  
33  
34  
35  
36 380  
37  
38  
39  
40  
41  
42  
43  
44  
45  
46  
47  
48  
49  
50  
51  
52  
53  
54  
55  
56  
57  
58  
59  
60

*(rigid-only alignment). Middle row: deformed CT scans. Bottom row: Difference map between registered scans (deformable registration) and template CT. In general, the registrations can successfully align the anatomy, but specific challenges arise in different body regions. Contrast in anatomical boundaries is fundamental to guide the registration, but clinical scan quality may vary. The boundary between liver and kidneys is less sharp in (a) than in (b), for example (top arrows), leading to poorer anatomical matching in this region; likewise, large deformations of the bladder are challenging to recover, where filling varies from (a) full to (b) empty (bottom arrows). Imaging artefacts can also be problematic, such as (c) motion artefacts (top arrow) and/or the use of contrast agents (bottom arrow). Note that high-intensity artefacts were masked out of the registration. Different disease cohorts have differences in image acquisition of parameters, patient positioning and imaged field-of-view ((d) brain tumour vs (e) abdominal neuroblastoma). Arrows indicate misregistration regions on the skeleton (d) and soft tissues (e).*

The average values for NCC was  $0.97 \pm 0.01$ , indicating a good match between deformed and template CTs.  $HU_{RMS}$  was  $94 \pm 10$  HU, which also indicates good global alignment. A level of difference in intensity is expected due to the variability in CT intensities between patients and the fuzzier aspect of the template CT. We also report a  $LVC_{avg}$  of  $0.38 \pm 0.16$ , which is indicative of the magnitude of volume changes that must be captured by the registrations, with the largest values being attributed to variations in patient size across the population studied.

### 3.2 Evaluation of anatomical and dose mapping

Figure 5 shows an example of the different CTs, contours and doses used in the evaluation of the anatomical and dose mapping.

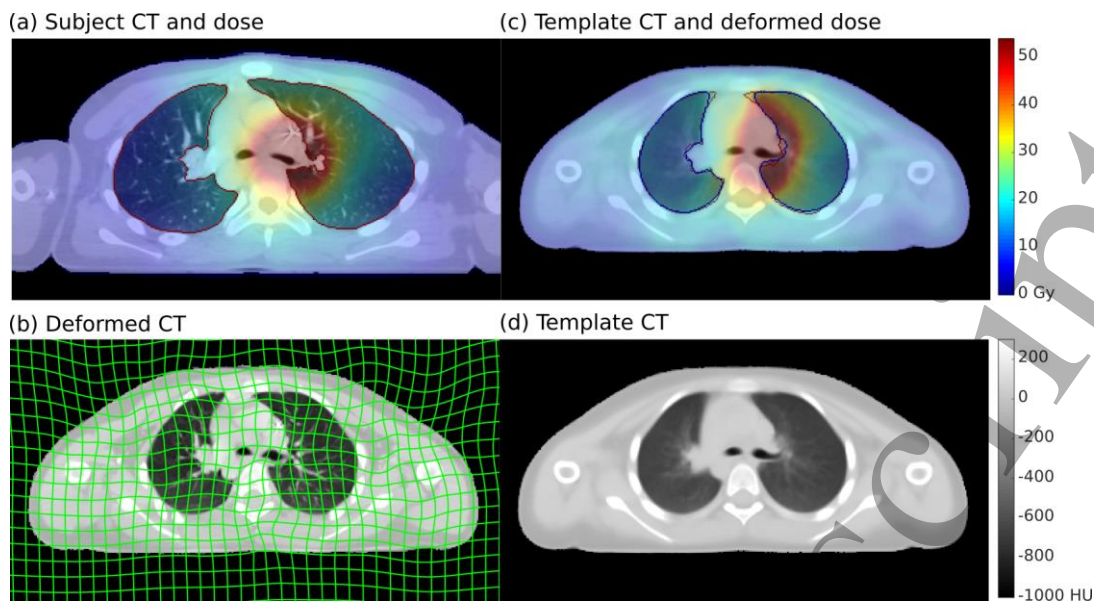


Figure 5- Example of data (images, contours and doses) used in the evaluation experiments. (a) CT, lungs contour (red) and dose distribution for one of the subjects included in the analysis (Ewing sarcoma); (b) Subject CT propagated to the template (affine followed by deformable registration), and corresponding deformation grid; (c) Template CT and lungs contour (blue), and overlaid deformed lungs contour (red) and deformed dose distribution; (d) Template CT by itself.

The quantities calculated for each organ are summarised in Table 2. Details of the distribution in volume and dose per organ within the patient group are also provided. Figure 6 complements this information by displaying the distribution of the DSC and RDA for all contours, chosen as representative measures of anatomical and dose mapping results.

Table 2- Quantitative evaluation of contour and dose deformation for different organs, expressed as mean  $\pm$  standard deviation.

Quantity	Volume of interest					
	CNS	Ocular globes	Lungs	Liver	Kidneys	Bladder
DSC	0.95 $\pm$ 0.05	0.85 $\pm$ 0.04	0.96 $\pm$ 0.01	0.91 $\pm$ 0.03	0.83 $\pm$ 0.06	0.65 $\pm$ 0.16
JC	0.92 $\pm$ 0.08	0.74 $\pm$ 0.06	0.92 $\pm$ 0.02	0.83 $\pm$ 0.5	0.71 $\pm$ 0.08	0.50 $\pm$ 0.16
DT <sub>avg</sub> (mm)	0.7 $\pm$ 1.0	0.9 $\pm$ 0.4	0.8 $\pm$ 0.3	2.7 $\pm$ 1.1	2.5 $\pm$ 1.3	7.1 $\pm$ 3.8
$\Delta$ TR (mm)	2.9 $\pm$ 5.7	1.7 $\pm$ 0.8*	1.3 $\pm$ 0.7*	4.9 $\pm$ 2.7	7.0 $\pm$ 4.5*	9.6 $\pm$ 4.6
RDA	0.02 $\pm$ 0.04	0.04 $\pm$ 0.04	0.05 $\pm$ 0.05	0.06 $\pm$ 0.03	0.09 $\pm$ 0.06	0.29 $\pm$ 0.28
D00	0.92 $\pm$ 0.07	0.75 $\pm$ 0.07	0.86 $\pm$ 0.05	0.81 $\pm$ 0.06	0.65 $\pm$ 0.09	0.36 $\pm$ 0.18

Number of subjects in analysis (no, %)	53 (100%)	34 (64%)	52 (98%)	49 (92%)	49 (92%)	49 (92%)
Volume (ml), median (range)	1331 (29 - 1891)	16 (10 - 21)	597 (49-2834)	645 (328 - 1632)	121 (62 - 284)	64 (10 - 350)
Mean organ dose (Gy), median (range)	23.6 (1.3 - 38.9)	26.2 (0.2 - 35.9)	3.5 (0 - 16.4)	6.7 (1.1 - 25.0)	5.2 (1.4 - 14.1)	1.1 (0 - 16.3)
<p>DSC = Dice Similarity Coefficient</p> <p>JC = Jaccard Coefficient</p> <p><math>DT_{avg}</math> = Average distance between surfaces</p> <p><math>\Delta TR</math> = Distance between centroids</p> <p>RDA = Relative difference of areas of DVHs</p> <p>D00 = Dose-organ overlap</p> <p>CNS = brain and spinal canal</p> <p>*For organs composed of two separate volumes, <math>\Delta TR</math> reported is the maximum value of the individual sub-volumes.</p>						

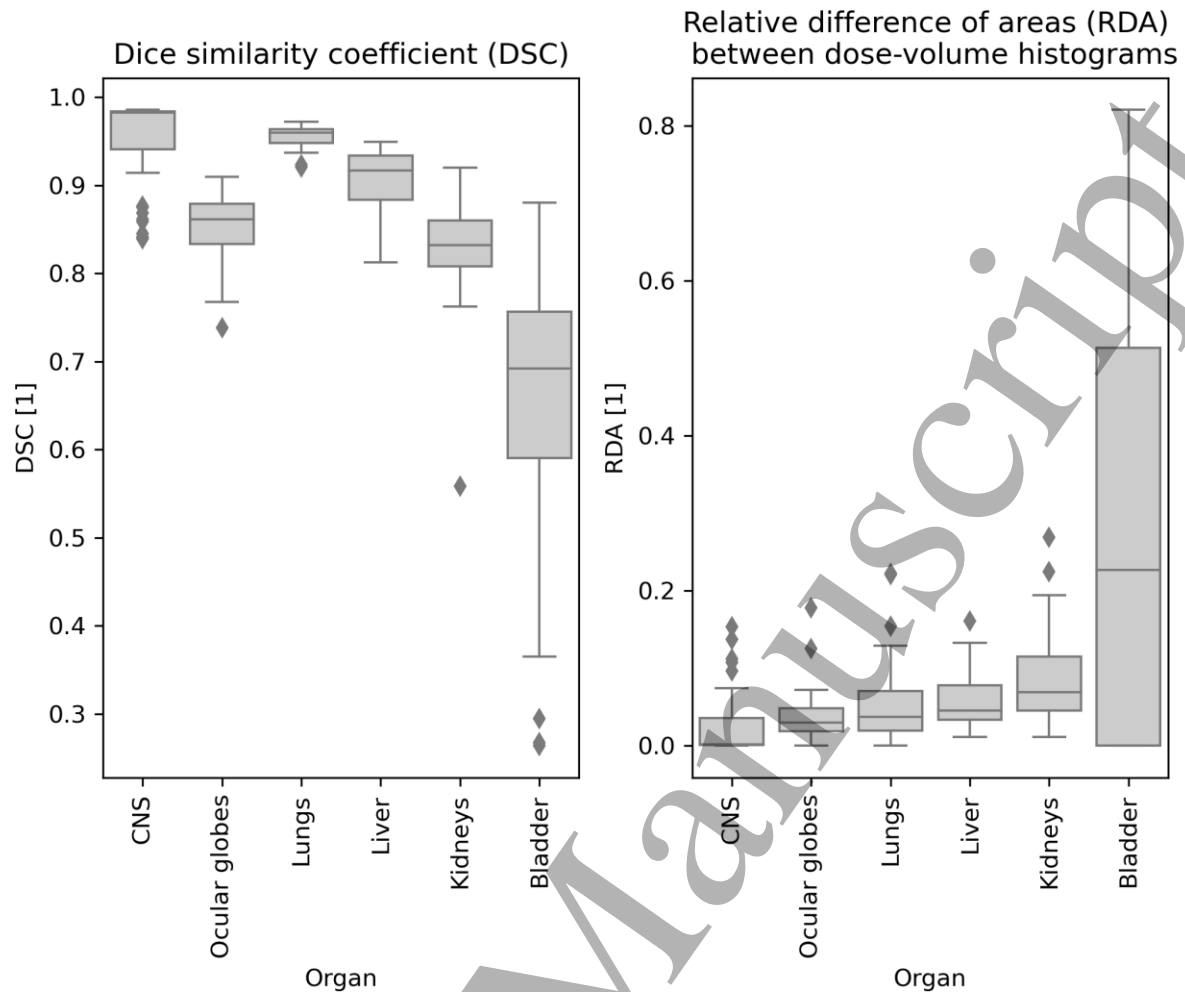


Figure 6- Boxplots for distribution of dice similarity coefficient (DSC) and relative difference of areas (RDA) after spatial normalisation. Subjects with contours defined available for analysis:  $N=\{53, 34, 52, 49, 49, 49\}$  for  $\{CNS, Ocular\ Globes, Lungs, Liver, Kidneys, Bladder\}$ . Outliers fall outside the  $\pm 2.7$  standard deviation range.

In general, better matching is found for organs in the head and thorax, than for those located in the abdomen and pelvis. The poorest performance was achieved in the bladder, the organ that exhibited the largest inter-subject volume variation due to differences in filling (excluding cases where other organs were partially imaged). Upon visual inspection of outliers for other regions of interest, the worst performances corresponded to abnormal anatomies, such as individuals with enlarged kidneys or inflammation in the lungs. A common error (affecting approximately 1 in 5 subjects) in CNS registration corresponded to misregistration of individual spinal vertebrae, which could lead to mismatch of the inferior end of the spinal canal (which was consistently defined at L3 for all subjects and template). Registrations also struggled with the kidney superior/inferior boundaries where contrast is poor, reflected in higher errors mapping the structure centroid. Registration quality was generally better for CSI than for other cohorts

1  
2  
3 420 (abdominal neuroblastoma, brain and Ewing's sarcoma). For example, the average DSC  
4 for the liver was  $0.92 \pm 0.02$  and  $0.88 \pm 0.03$  for CSI and other cohorts, respectively.  
5 Considering CSI subjects only, we also investigated the relationship between all metrics  
6 and absolute age difference (relative to the template CT). We did not find any strong  
7 evidence that subjects with ages furthest away from average were better registered to the  
8  
9  
10 425 template CT. When pooling data for all organs and subjects, the Pearson's correlation  
11 coefficients were  $-0.05$ ,  $-0.04$ ,  $0.08$ ,  $0.04$ ,  $0.04$  and  $-0.04$  ( $p > 0.05$ ) for DSC, JC,  $DT_{avg}$ ,  $\Delta TR$ , RDA  
12 and D00, respectively, showing a weak correlation between age similarity and  
13 anatomical/dose mapping to the template CT.  
14  
15  
16  
17

### 18 430 3.3 Additional evaluation experiments

19  
20  
21  
22 Separately to the previous experiments, we also evaluated anatomical and dose  
23 mapping to the template for the twenty subjects used in the atlas construction. We found  
24 no strong statistical evidence that the measured quantities were better for CSI subjects  
25 used for atlas construction than for those used only for evaluation ( $p > 0.05$ , Wilcoxon rank  
26 435 sum test).  
27  
28

29  
30 The anatomical and dose mapping achieved with other choices of common  
31 reference space was also assessed, and compared to the proposed template CT. First, we  
32 calculated all metrics when spatially normalising to a population-representative individual.  
33  
34 440 The chosen individual was the subject closest to the average age, also used for atlas  
35 construction. Then, we repeated the same analysis but choosing as reference the youngest  
36 and oldest subjects (proxy for least representative subjects) to highlight the importance of  
37 adequate reference selection for spatial normalisation. Results are shown in Table 3 when  
38 pooling data for all organs and subjects. Figure 7 showcases the differences in DSC for all  
39 organs when comparing spatial normalisation to the template CT and representative  
40  
41 445 organs when comparing spatial normalisation to the template CT and representative  
42 subject only. Spatial normalisation to a representative subject generally resulted in poorer  
43 metrics achieved in comparison to the template CT but improved against using as  
44 reference space subjects with more dissimilar ages (and hence expected to be less  
45 representative of the population).  
46  
47

48  
49 450 Finally, to evaluate the impact of initial template selection in the atlas constructed,  
50 the atlas construction process was repeated by iterating the initial template selected over  
51 the remaining nineteen subjects. All atlases generated were comparable to the proposed  
52 atlas after affine registration ( $NCC = 0.993 \pm 0.003$  and  $HU_{RMS} = 45 \pm 9$  HU), irrespective of  
53 which subject was used to initiate the process. Visually, the inter-atlas anatomical  
54 variability was small in comparison with the inter-subject variability presented in the  
55  
56 455 patient group. Furthermore, all anatomical and dose mapping metrics were recalculated  
57 on two (out of nineteen) of these comparable atlases, the ones constructed using the  
58 youngest and oldest subjects as the initial reference. Similar metrics were found on the  
59  
60

three different template CTs analysed, demonstrating the robustness of the atlas construction process. These results are also summarised in Table 3 and Figure 7.

*Table 3- Quantitative evaluation of contour and dose deformation to different common reference spaces: proposed template CT (evaluated in Sections 3.1 and 3.2), population individuals (youngest, average and oldest in age), and template CTs generated with different initial template (youngest and oldest subjects). Data pooled for all organs and subjects. Expressed as mean  $\pm$  standard deviation. Note how similar results are achieved for all template CTs; representative subject is associated with poorer metrics but outperforms the less representative individuals.*

Quantity	Template CT	Other common reference spaces				
		Individuals			Template CT with different initialisation	
		Average	Youngest	Oldest	Youngest	Oldest
DSC	0.86 $\pm$ 0.13	0.83 $\pm$ 0.15	0.75 $\pm$ 0.23	0.81 $\pm$ 0.14	0.86 $\pm$ 0.13	0.86 $\pm$ 0.13
JC	0.77 $\pm$ 0.17	0.74 $\pm$ 0.19	0.64 $\pm$ 0.26	0.70 $\pm$ 0.18	0.78 $\pm$ 0.17	0.78 $\pm$ 0.17
DT <sub>avg</sub> (mm)	2.5 $\pm$ 2.8	2.7 $\pm$ 3.1	3.9 $\pm$ 3.8	4.6 $\pm$ 4.3	2.5 $\pm$ 2.8	2.4 $\pm$ 2.9
$\Delta$ TR (mm)	4.6 $\pm$ 4.8	5.6 $\pm$ 6.0	8.4 $\pm$ 7.1	9.4 $\pm$ 8.2	4.6 $\pm$ 4.8	4.5 $\pm$ 4.8
RDA	0.09 $\pm$ 0.15	0.11 $\pm$ 0.17	0.12 $\pm$ 0.17	0.10 $\pm$ 0.13	0.10 $\pm$ 0.15	0.10 $\pm$ 0.15
DOO	0.73 $\pm$ 0.21	0.69 $\pm$ 0.07	0.62 $\pm$ 0.27	0.66 $\pm$ 0.21	0.73 $\pm$ 0.21	0.73 $\pm$ 0.21

470

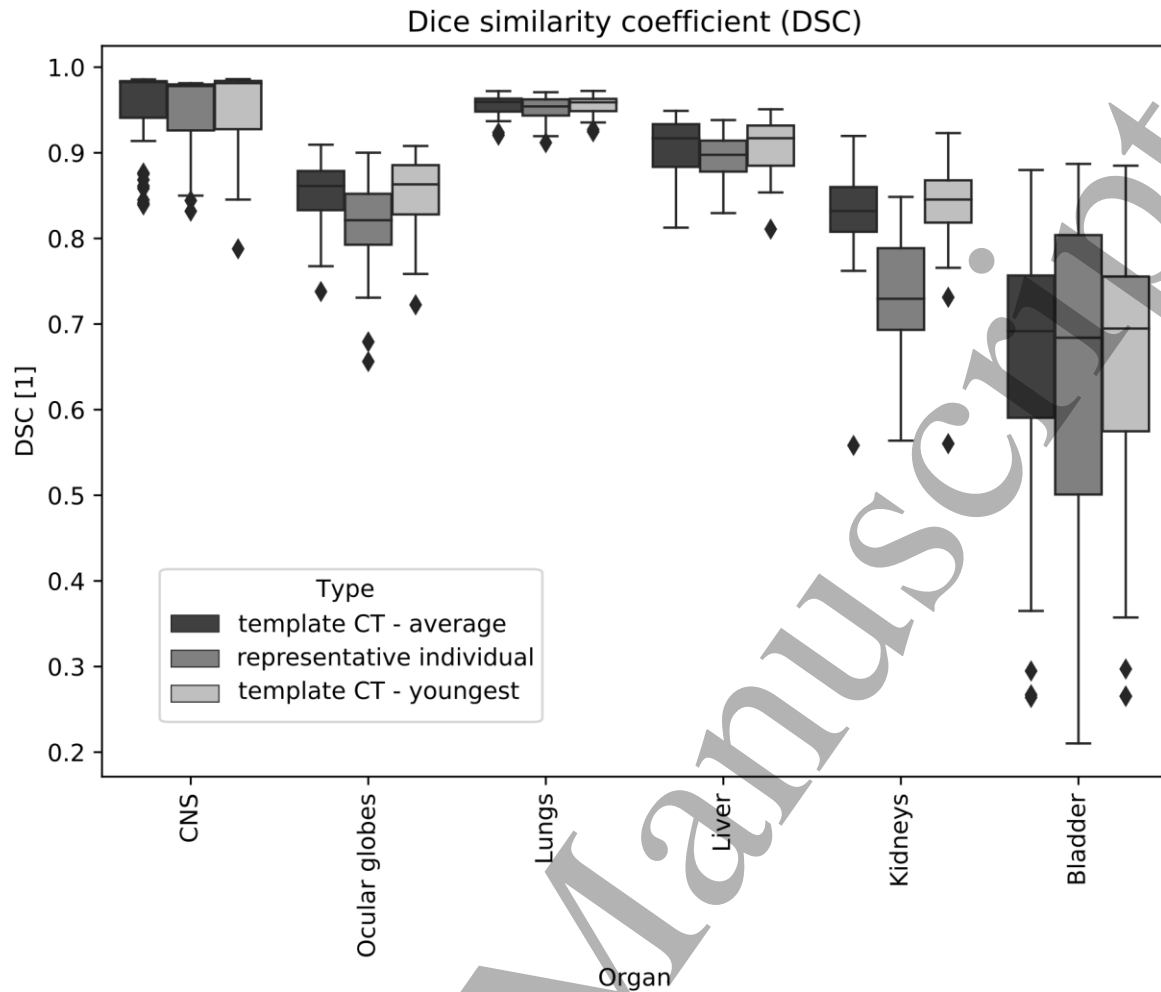


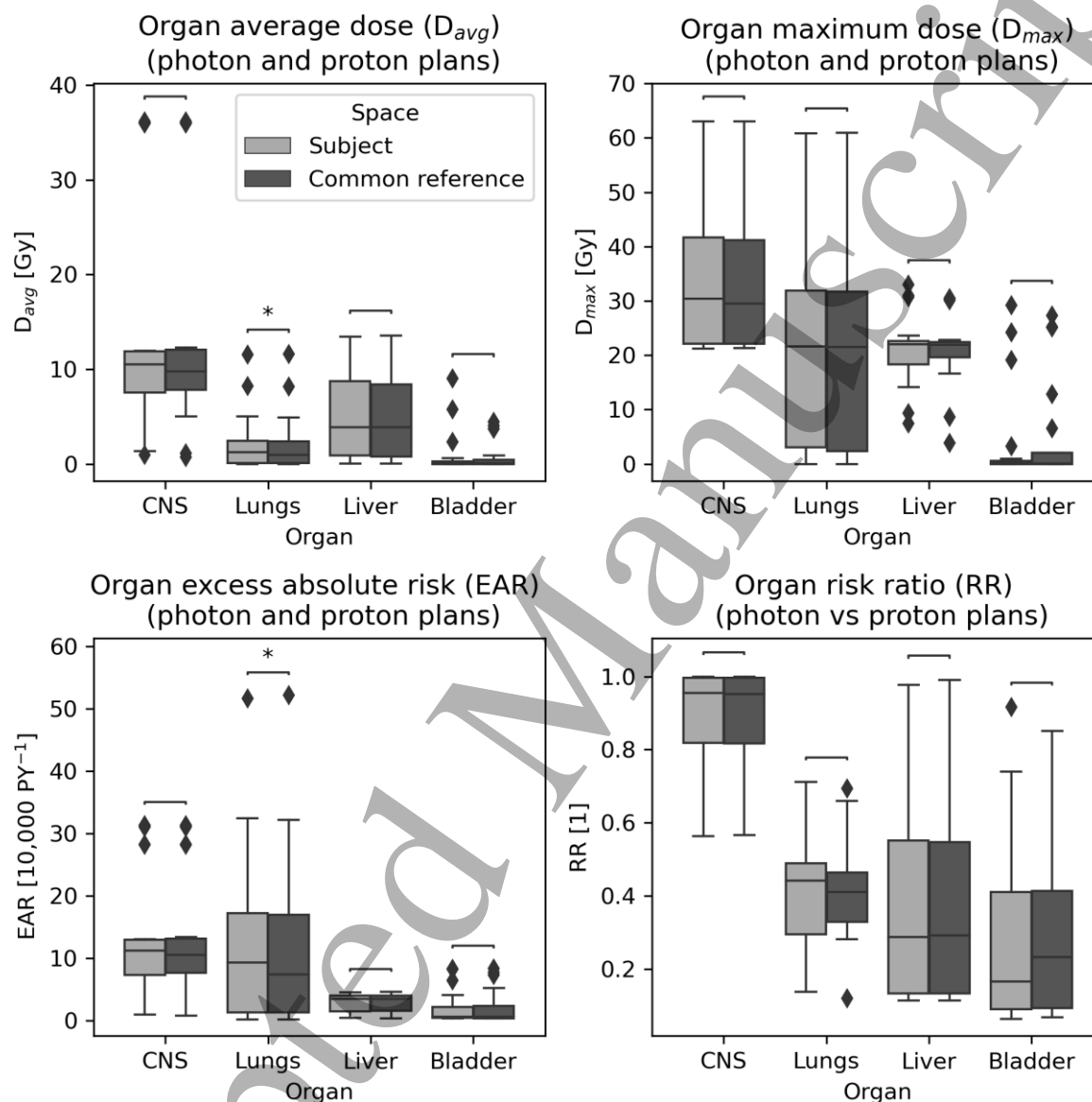
Figure 7- Boxplots for distribution of dice similarity coefficient (DSC) after spatial normalisation comparing different common reference spaces: proposed template CT, representative population individual, and templates CT generated with a different initial template (youngest subject). Subjects with contours defined available for analysis:  $N = \{53, 34, 52, 49, 49, 49\}$  for  $\{\text{CNS}, \text{Ocular Globes}, \text{Lungs}, \text{Liver}, \text{Kidneys}, \text{Bladder}\}$ . Outliers fall outside the  $\pm 2.7$  standard deviation range. Note how similar results are achieved for both template CTs, with higher metrics found relative to the representative subject.

### 3.4 Evaluation of a common reference space to facilitate the study of radiation-induced second malignant neoplasms

The radiation-induced SMN risk from photon and proton therapy treatments was estimated by propagating the dose onto the template CT and contours (subject to common reference space), and by using the dose on the native CTs and contours (subject space) (Figure 8). There was no strong evidence of statistically significant differences in the  $D_{\text{avg}}$ ,  $D_{\text{max}}$ , EAR and RR calculated on the two spaces (Wilcoxon paired signed rank tests, p-values

1  
2  
3  
4  
5  
6 490  
7  
8  
9  
10  
11  
12  
13  
14  
15  
16  
17  
18  
19  
20  
21  
22  
23  
24  
25  
26  
27  
28  
29  
30  
31  
32  
33  
34  
35  
36  
37  
38  
39  
40  
41  
42  
43  
44  
45  
46  
47  
48  
49  
50  
51  
52  
53  
54  
55  
56  
57  
58  
59  
60

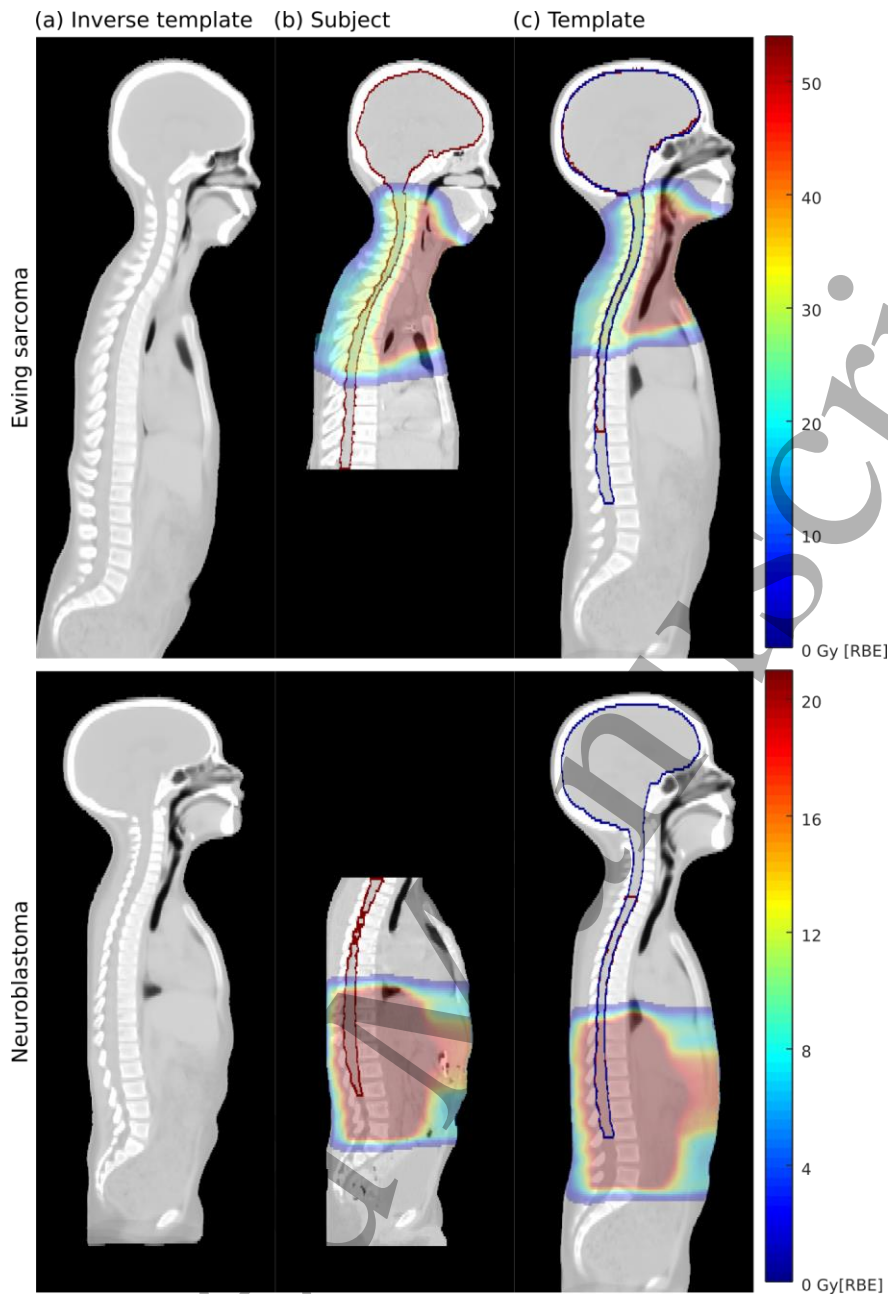
>0.05 for the majority of data pairs). This suggests that analysis on the common reference or subject space is equivalent for DVH-based studies and the added uncertainties to dose-volume characteristics associated with the spatial normalisation have a small impact on the population level.



495  
50  
51  
52  
53  
54  
55  
56  
57  
58  
59  
60

Figure 8- (a) Average dose ( $D_{avg}$ ), (b) Maximum dose ( $D_{max}$ ) and (c) Excess Absolute Risk (EAR) calculated for CNS, lungs, liver and bladder considering both photon and proton therapy plans, and corresponding (d) Risk Ratio (RR) between the two modalities calculated using the dose onto the template CT and contours (subject to common reference space), and by using the dose on the native CTs and contours (subject space). Subjects with contours defined available for analysis:  $N = \{14, 13, 10, 10\}$  for {CNS, Lungs, Liver, Bladder}. Outliers fall outside the  $\pm 2.7$  standard deviation range. Asterisks indicate  $p < 0.05$  for Wilcoxon paired signed rank tests.

1  
2  
3  
4  
5 In Figure 9 we showcase examples of proton plans for paediatric Ewing sarcoma and  
6 neuroblastoma to highlight the potential benefits of using the common reference space for  
7 SMN risk modelling and analysis. While prescription is very different between cohorts, both  
8 505 treatments irradiate the spine at similar dose levels (estimated  $V_{20Gy}$  to the CNS of 3.1%  
9 and 2.3%, respectively) but at distinct sub-regions. Propagating dose to a common  
10 template space allows to explore how such spatial relationships may impact the  
11 relationships between dose and clinical end-points. Furthermore, the template CT and its  
12 contours (blue) allow for DVH-based analysis in the absence of segmentations on the  
13 subject CT (red) and to account for volume effects when only partial volumes were imaged.  
14 510 For example, in the neuroblastoma case the absolute EAR for the CNS would be 12.9 per  
15 10,000 person-years if not properly accounting for partial imaging of this organ (i.e., brain  
16 is outside the imaged region); 0.54 per 10,000 person-years is the estimated absolute  
17 value in the template space. Note that when calculating EAR shown in Figure 8, we only  
18 used the common field-of-view between subject and template for a fairer comparison.  
19 Finally, the template CT may be used to generate virtual phantoms to estimate out-of-field  
20 doses. A possible way of doing this is by using the patient-specific inverse deformations to  
21 generate a patient-specific phantom.  
22 515  
23  
24  
25  
26  
27  
28  
29  
30 520  
31  
32  
33  
34  
35  
36  
37  
38  
39  
40  
41  
42  
43  
44  
45  
46  
47  
48  
49  
50  
51  
52  
53  
54  
55  
56  
57  
58  
59  
60



44  
45  
46  
47  
48  
49  
50  
51  
52  
53  
54  
55  
56  
57  
58  
59  
60

525  
530

*Figure 9- Two clinical cases demonstrating the advantages of dose analysis on the template CT (top: Ewing sarcoma; bottom: neuroblastoma). Propagating dose from subject space (b) to the common reference space (c) allows to explore the spatial relationships between dose and clinical end-points – for example, both cases irradiate comparable spinal volumes with 20 Gy or more, but at distinct anatomical regions. Furthermore, the template contour (blue) allows for DVH-based analysis in the absence of patient-specific segmentations (red) and to account for volume effects when only partial volumes were imaged. Finally, the template CT may be used to generate virtual phantoms to estimate out-of-field doses by, for example, using the patient-specific inverse deformations (a).*

#### 4. DISCUSSION

In this study, we investigated the feasibility of atlas-construction and spatial normalisation to facilitate voxel-based analysis of radiation-induced toxicities in paediatric radiotherapy patients. This methodology exploits imaging and contour segmentation information from a CSI cohort to spatially standardise the heterogeneous paediatric population and facilitate subsequent analysis. The methodology was applied to paediatric CSI, abdominal neuroblastoma, Ewing sarcoma and brain tumour patients. The single synthetic template generated was able to satisfactorily account for considerable variability in age and gender. This demonstrates the potential of spatial normalisation of a heterogeneous population to facilitate subsequent analysis of varied clinical end-points in larger paediatric populations. To the best of our knowledge, this is the first-time atlas construction and spatial normalisation were investigated for whole-body images of paediatric cancer patients who underwent radiotherapy.

We chose for atlas construction the CSI patient group for its potential as a reference frame, as the radiation fields used cover many organs and tissues. CSI is routinely used in the treatment of medulloblastomas, a relatively common tumour type that can occur across all ages of development which also facilitates data availability. Treatment positioning is supine and consistent across patients, reducing variability in pose. In this cohort the gross tumour is usually resected prior to radiotherapy and hence not visible on CT, minimising potential issues that variable gross tumour positions could cause on the atlas construction. A limitation is that shunts and, particularly for younger patients, intubation are commonly used, adding external elements and artefacts to the CTs. While we have demonstrated that other cohorts can be satisfactory overlaid on the template CT, registration quality metrics were higher for CSI subjects likely due to the increased similarity in terms of setup and presentation. The patients in non-CSI cohorts were also younger on average and hence it is possible that larger deformations had to be captured. Other cohorts will also have unique characteristics not commonly found in the CSI cohort. For example, excessive gas in the bowel is observed commonly in abdominal neuroblastoma patients (Lim *et al*/2020), increasing the challenges in co-registering these images to a CSI-based template.

The methodology's success in spatially normalising radiotherapy data depends on the accuracy achieved in inter-subject DIR. The paediatric population is particularly challenging to co-register. Large deformations must be captured to co-register subjects across development stages, which poses a complex challenge to DIR due to inter-subject variability across sex, age, height, weight, internal anatomy and abnormalities caused by disease. These challenges differ between anatomical regions. Volumes in the abdomen and pelvis are highly deformable and, due to physiological motion, one-to-one mapping does not always exist, making the registrations very challenging. Indeed, we found better

1  
2  
3 spatial mapping for organs in head and thorax (DSC of  $0.95\pm 0.05$ ,  $0.85\pm 0.04$  and  
4  $0.96\pm 0.01$  for CNS, ocular globes and lungs) than in other regions ( $0.91\pm 0.03$ ,  $0.83\pm 0.06$   
5 and  $0.65\pm 0.16$  for liver, kidneys and bladder). The poorest performance was in the bladder,  
6 a highly deformable organ: 50% of the subjects had a DSC below 0.7. For reference,  
7  
8  
9 575 American Association of Physicists in Medicine (AAPM) commissioned Task Group 132  
10 suggest a DSC of 0.8 - 0.9 as being good performance for image registration (Brock *et al*  
11 2017). However, it must be noted that DSC is higher for larger volumes and interpretation  
12 of the absolute values must always consider the absolute organ volumes. RDA and D00  
13 ranged between  $0.02\pm 0.04$  -  $0.29\pm 0.28$  and  $0.36\pm 0.18$  -  $0.92\pm 0.07$ , respectively, for the  
14  
15  
16 580 same contours. These are comparable to values reported in other studies. In a recent  
17 study, Pilia *et al*/report DSC of  $0.80\pm 0.11$ ,  $0.44\pm 0.23$ , and  $0.58\pm 0.14$  for liver, kidneys and  
18 bladder, respectively, when using Elastix groupwise to co-register adults whole body MRIs  
19 (Pilia *et al*/2019). Acosta *et al* report RDA and D00 of  $0.09\pm 0.05$  and  $0.64\pm 0.1$  for spatial  
20 normalisation of rectum dose (Acosta *et al*/2013). Monti *et al*/report a D00 in the range  
21  
22  
23 585  $0.39\pm 0.11$  -  $0.58\pm 0.10$  for brain dose sub-volumes (Monti *et al*/2020).

24  
25 We consider our results promising, particularly when taking into consideration that  
26 we are using a general-purpose registration methodology, the task of inter-subject  
27 registration is very challenging, and the fact that we are dealing with whole-body images.  
28 Nevertheless, more specialised approaches should be explored in the future, particularly  
29  
30  
31 590 to improve matching in highly deformable organs (e.g., bladder) or when there is no true  
32 one-to-one mapping (e.g., regions of bowel gas). For example, by using additional *a priori*  
33 structural information (i.e., landmarks or contours) to guide the registration such that large  
34 local deformations can be better captured (Johnson and Christensen 2002, Rivest-Hénault  
35 *et al*/2014). Further work is also needed to evaluate the atlas constructed using more  
36  
37  
38 595 comprehensive datasets, with more organs and numbers of patient per cohort, ideally from  
39 multiple institutions.

40  
41 One of the most promising applications of spatial normalisation is to develop voxel-  
42 based risk models of late effects that account for heterogeneous spatial radiosensitivity,  
43 which can potentially be used to develop personalized risk-guided therapies. This is an  
44  
45  
46 600 emerging area in radiation toxicities research (Palma *et al*/2020). Other groups have  
47 investigated voxel-based analysis to identify radiosensitive subregions of organs (such as  
48 bladder, rectum, lungs and head and neck) in adult cohorts, which can then be avoided  
49 during RT planning (Acosta *et al*/2013, Palma *et al*/2016, Monti *et al*/2017, McWilliam *et al*  
50 2017, Beasley *et al*/2018). Palma *et al*/introduced recently the concept of comprehensive  
51  
52  
53 605 NTCP models that include full spatial information of the dose distributions (Palma *et al*  
54 2019a). The present study is the first step toward voxel-based analysis in radiation-induced  
55 toxicities after paediatric radiotherapy. Our next step is to use the proposed methodology  
56 to explore the dose-response relationships for paediatric late effects.  
57  
58  
59  
60

1  
2  
3 The spatial normalisation process was evaluated in our study at the organ level,  
4 which is the level of accuracy historically used in radiation-induced toxicity analysis. Our  
5 610 results indicate similar normal tissue complication probability (NTCP) models can be  
6 generated using the common reference or native spaces. For voxel-based analysis  
7 applications, validation of spatial mapping at sub-structures and/or voxel level is required  
8 but it is a challenging problem, particularly for homogeneous organs with few imaging  
9 features. Further work is therefore required to evaluate and improve registrations at finer  
10 resolutions. For example, this could be done by evaluating the accuracy of mapping  
11 615 anatomical landmarks, or by dividing organs into well-defined sub-structures that can be  
12 analysed separately. Improving localised mapping is increasingly relevant for clinical  
13 endpoints such as brain injury (Gunther *et al*/2015, Viselner *et al*/2019), lung fibrosis (Veiga  
14 620 *et al*/2018) and heart failure (McWilliam *et al*/2017). We recommend that in clinical studies  
15 investigating organ-specific end-points additional validation is performed accordingly.  
16 Better soft tissue mapping may be achievable by incorporating complementary multimodal  
17 imaging such as MRI (Monti *et al*/2020), or by digitally enhancing the CT images to improve  
18 contrast. Furthermore, we would like to highlight that achieving adequate voxel-level  
19 625 mapping allows one to potentially develop radiation-induced toxicity predictive models  
20 that consider simultaneously with the local dose, the localised tissue radiosensitivity which  
21 can be measured with co-registered multimodal functional imaging (Yankeelov *et al* 2014).  
22 In the paediatric population, accounting for patient-specific radiosensitivity is particularly  
23 important as spurts of growth are occurring as part of the normal development into  
24 adulthood.  
25 630

26 While the methodology is not specific to this clinical endpoint and can be adapted  
27 to other endpoints, in our opinion it is very promising in the study of radiation-induced  
28 SMNs. The use of the template CT for analysis addresses some of the challenges associated  
29 with this end-point:  
30

31 635 (1) spatial normalisation brings the opportunity to understand the SMN dose-response  
32 as function of the local dose instead of dose to volume (e.g. average dose) and  
33 potentially identify sub-regions of increased radiosensitivity.

34 (2) the methodology generates standardised whole-body organ segmentations that  
35 are often missing from routine clinical data (i.e. atlas-based segmentation). This has  
36 advantages even for traditional DVH-based modelling where manual segmentation  
37 becomes prohibitive for large numbers of subjects. Manual segmentation is associated  
38 640 with variability between clinicians and is challenging to deploy practically on larger  
39 datasets as several organs relevant to SMN risk are not segmented clinically due  
40 limited clinical resources.

41 645 (3) the template CT can be used to account for missing anatomical information, as it  
42 can be used to estimate out-of-field doses and volumes (i.e. population-representative  
43 virtual phantom). Typically, the planning CT images do not cover the whole-body (only  
44  
45  
46  
47  
48  
49  
50  
51  
52  
53  
54  
55  
56  
57  
58  
59  
60

1  
2  
3 treated regions), which complicates studying out-of-field effects. The template CT built  
4 from the CSI cohort covers all organs and therefore can be used as radiotherapy-  
5 specific synthetic phantom to estimate of anatomy and out-of-field doses. In this case,  
6 650 it is increasingly important to investigate age and gender-specific templates. The use  
7 of computational and/or physical phantoms is common in radiation dosimetry,  
8 although these are usually built from healthy individuals (Segars *et al* 2009, Christ *et*  
9 *al* 2009, Lee *et al* 2015, Xie *et al* 2017).

10  
11  
12  
13 655 (4) the template CT is whole-body and hence allows us to harness routine dose-volume  
14 information from patient groups which were irradiated at different sites, making the  
15 most of partial information and allowing to understand the dose-response at different  
16 dose levels (i.e., inside the RT target, near-target and out-of-field).

17  
18  
19  
20  
21 660 Choosing a representative common reference space is a key step for spatial  
22 normalisation. The template CT proposed was constructed using groupwise image  
23 registration to reduce bias associated with the choice of the common reference space in  
24 subsequent analysis. The choice of image used to initialise the atlas construction process  
25 can still bias the final template generated (Agier *et al* 2020); however, the differences we  
26 found when varying the initialisation were small. To the best of our knowledge, using  
27  
28 665 population-specific average atlases for radiotherapy applications, as in our study, had not  
29 been investigated before in the literature of radiation-induced toxicities. The typical  
30 approach is to define an individual from the population as the single template. This can be  
31 empirically performed - for example, manually by visual inspection (Beasley *et al* 2018) or  
32 choosing a subject with mean/median anatomical features (Palma *et al* 2016, Monti *et al*  
33 670 2017, Mylona *et al* 2019). We report poorer anatomical and dose mapping metrics using  
34 this simpler approach than for the average atlas. Another method is to use less biased  
35 methods of identifying the population's most representative individual - for example, using  
36 clustering approaches (Acosta *et al* 2013, Marcello *et al* 2020). There are a variety of  
37 methods proposed for optimal atlas selection developed in the context atlas-based  
38 segmentation (Rohlfing *et al* 2004, Aljabar *et al* 2007, Zhou *et al* 2014, Iglesias and  
39 Sabuncu 2015). Others have used well-established anatomical atlases developed for  
40 neuroimaging applications (Monti *et al* 2020) or virtual anatomies (Palma *et al* 2019b).  
41 These templates are theoretically easier to share between institutions and facilitate  
42 standardisation of how spatial analysis is performed across studies; however, they are not  
43 675 necessarily representative of the populations analysed. With this in mind, we aim to make  
44 our model available in the future to facilitate other studies in paediatric late effects  
45 (<https://cmic-rt.github.io/RT-PAL/>). The bias in atlas selection and subsequent voxel-based  
46 analysis of toxicity can be mitigated by repeating analysis on multiple references to verify  
47 if similar spatial patterns arise even when the common reference space varies (Dréan *et*  
48 *al* 2016, Marcello *et al* 2020, McWilliam *et al* 2020).  
49  
50 680  
51  
52  
53  
54  
55  
56  
57  
58  
59  
60

1  
2  
3 We used a general-purpose, well-established groupwise registration tool, tailored  
4 to better deal with the challenges in co-registering the CSI paediatric cancer population.  
5 More efficient approaches could be explored, both in terms of memory requirements and  
6 to better deal with co-registering heterogenous datasets. Groupwise image registration is  
7 a popular methodology in human brain studies (Dickie *et al*/2017); whole-body studies like  
8  
9 690 a popular methodology in human brain studies (Dickie *et al*/2017); whole-body studies like  
10 ours are still rare due to challenges in registering heterogeneous large datasets of high  
11 resolution images (Pilia *et al* 2019, Agier *et al* 2020). While the template constructed  
12 effectively represented both genders and a wide range of ages for demonstration  
13 purposes, it is admittedly a simplified approach not able to fully account for the anatomical  
14 variation in heterogeneous populations. Multiple (age and gender-specific) templates may  
15  
16 695 be constructed with larger datasets. Accounting for anatomical differences between  
17 genders is relevant as side-effects can be gender-specific (for example, second breast  
18 cancers (Inskip *et al* 2009)). The benefits of age-appropriate atlases have been  
19 demonstrated in neuroimaging applications (Fonov *et al* 2011). While the quality of  
20 mapping may be improved by splitting the population into sub-groups using several, more  
21 refined atlases, this will also reduce how generalisable the methodology and subsequent  
22 findings are. Hence a single representative template is an attractive approach, particularly  
23  
24 700 in rare populations (such as paediatric cancers) where it is more challenging to gather  
25 large datasets. Alternatively, atlas synthesis has been proposed using hierarchical imaging  
26 clustering to form a pyramid of classes (Wang *et al*/2010). Alternative strategies may help  
27 with the challenges in co-registering whole-body images and scaling to larger datasets, by  
28 using deep-learning to speed up the processes (Ahmad *et al* 2019) or by avoiding dense  
29 registration (Agier *et al* 2020).  
30  
31 705

32  
33  
34  
35  
36  
37  
38 710 Despite the associated challenges, methodologies focused on whole-body imaging  
39 have the potential of enabling risk prediction in big data studies. Examples of the potential  
40 applications that leverage three-dimensional whole-body population data are discussed in  
41 detail by Strand *et al* and include anomaly detection, group comparisons, longitudinal  
42 analysis and correlation analysis (Strand *et al*/2017). Similar ideas were recently explored  
43 in the context of radiotherapy toxicity predictive modelling for liver stereotactic ablative  
44 radiotherapy (Ibragimov *et al* 2018, 2019). These studies harnessed the potential of  
45  
46 715 artificial intelligence and spatial normalisation to a common reference space to combine  
47 complex three-dimensional imaging and non-imaging data to build predictive models of  
48 radiotherapy outcomes.  
49

50  
51  
52  
53 720 Finally, detailed long-term data collection is essential to understand and minimise  
54 adverse effects of radiotherapy. Single institutions have limited ability to gather adequate  
55 data due to the rarity of childhood cancers. Late effects such as SMNs have long latency  
56 periods which make data collection challenging (Armstrong *et al*/2009, Bhakta *et al*/2017).  
57 The need for comprehensive, multi-institutional collection of dosimetry and follow up data  
58 is recognized by the paediatric radiotherapy community, with on-going initiatives to  
59  
60

1  
2  
3 725 combine efforts to accelerate outcomes-based research toward patient benefit (Berrington  
4 de Gonzalez *et al* 2017). An example of such initiatives is the Paediatric Proton/Photon  
5 Consortium Registry (PPCR), a consented registry with 15 institutions that has been  
6 collating detailed baseline, treatment and follow-up information since 2012, including  
7 planning CT images and dosimetry (Lawell *et al*/2019). The methodology developed in this  
8  
9  
10 730 work aims to leverage complex 3D data and facilitate analysis in such emerging rich  
11 datasets and clinical trials data.  
12  
13  
14  
15

## 16 5. CONCLUSIONS

17  
18  
19 735 In this work, we proposed and evaluated atlas construction and spatial  
20 normalisation in paediatric radiotherapy CTs. An atlas-based template CT model  
21 representative of the paediatric cancer population was developed using groupwise image  
22 registration. Spatial normalisation to this template CT was evaluated with promising  
23 results, indicating it is possible to spatially standardise the paediatric radiotherapy  
24 populations despite considerable variability in age and gender. The proposed  
25 methodological framework leverages deformable image registration to enable modelling  
26 and validation of dose-response relationships in paediatric radiotherapy. This study is the  
27 740 first step toward voxel-based analysis in radiation-induced toxicities following paediatric  
28 radiotherapy.  
29  
30  
31  
32  
33

34 745

## 36 REFERENCES

- 37  
38  
39  
40 Acosta O, Drean G, Ospina J D, Simon A, Haigron P, Lafond C and De Crevoisier R 2013  
41 Voxel-based population analysis for correlating local dose and rectal toxicity in  
42 prostate cancer radiotherapy *Phys. Med. Biol.* **58** 2581-95  
43 750  
44  
45 Agier R, Valette S, Kéchichian R, Fanton L and Prost R 2020 Hubless keypoint-based 3D  
46 deformable groupwise registration *Med. Image Anal.* **59** 101564  
47  
48  
49 Ahmad S, Fan J, Dong P, Cao X, Yap P-T and Shen D 2019 Deep Learning Deformation  
50 Initialization for Rapid Groupwise Registration of Inhomogeneous Image  
51 Populations *Front. Neuroinformatics* **13** Online:  
52 755 <https://www.frontiersin.org/articles/10.3389/fninf.2019.00034/full>  
53  
54  
55  
56 Aljabar P, Heckemann R, Hammers A, Hajnal J V and Rueckert D 2007 Classifier Selection  
57 Strategies for Label Fusion Using Large Atlas Databases *Medical Image Computing*  
58 *and Computer-Assisted Intervention - MICCAI 2007 Lecture Notes in Computer*  
59  
60

- 1  
2  
3 760 Science ed N Ayache, S Ourselin and A Maeder (Berlin, Heidelberg: Springer) pp  
4 523-31  
5  
6  
7 Arain A, Herman T and Matthiesen C 2015 Late Effects of Radiation Therapy in Pediatric  
8 Cancer Survivors *J. Okla. State Med. Assoc.* **108** 129-35  
9  
10  
11 Armstrong G T, Liu Q, Yasui Y, Neglia J P, Leisenring W, Robison L L and Mertens A C 2009  
12 765 Late Mortality Among 5-Year Survivors of Childhood Cancer: A Summary From the  
13 Childhood Cancer Survivor Study *J. Clin. Oncol.* **27** 2328-38  
14  
15  
16 Beasley W, Thor M, McWilliam A, Green A, Mackay R, Slevin N, Olsson C, Pettersson N,  
17 Finizia C, Estilo C, Riaz N, Lee N Y, Deasy J O and van Herk M 2018 Image-based  
18 Data Mining to Probe Dosimetric Correlates of Radiation-induced Trismus *Int. J.*  
19 770 *Radiat. Oncol.* **102** 1330-8  
20  
21  
22  
23 Berrington de Gonzalez A, Vikram B, Buchsbaum J C, de Vathaire F, Dörr W, Hass-Kogan  
24 D, Langendijk J A, Mahajan A, Newhauser W, Ottolenghi A, Ronckers C, Schulte R,  
25 Walsh L, Yock T I and Kleinerman R A 2017 A Clarion Call for Large-Scale  
26 Collaborative Studies of Pediatric Proton Therapy *Int. J. Radiat. Oncol.* **98** 980-1  
27  
28  
29  
30 775 Bhakta N, Liu Q, Ness K K, Baassiri M, Eissa H, Yeo F, Chemaitilly W, Ehrhardt M J, Bass J,  
31 Bishop M W, Shelton K, Lu L, Huang S, Li Z, Caron E, Lanctot J, Howell C, Folse T,  
32 Joshi V, Green D M, Mulrooney D A, Armstrong G T, Krull K R, Brinkman T M, Khan  
33 R B, Srivastava D K, Hudson M M, Yasui Y and Robison L L 2017 The Cumulative  
34 Burden of Surviving Childhood Cancer: An Initial Report from the St. Jude Lifetime  
35 Cohort Study *Lancet Lond. Engl.* **390** 2569-82  
36  
37 780  
38  
39 Brock K K, Mutic S, McNutt T R, Li H and Kessler M L 2017 Use of image registration and  
40 fusion algorithms and techniques in radiotherapy: Report of the AAPM Radiation  
41 Therapy Committee Task Group No. 132 *Med. Phys.* **44** e43-76  
42  
43  
44  
45 Cancer Research UK 2015 Children's cancer statistics *Cancer Res. UK* Online:  
46 785 [http://www.cancerresearchuk.org/health-professional/cancer-statistics/childrens-](http://www.cancerresearchuk.org/health-professional/cancer-statistics/childrens-cancers)  
47 [cancers](http://www.cancerresearchuk.org/health-professional/cancer-statistics/childrens-cancers)  
48  
49  
50 Christ A, Kainz W, Hahn E G, Honegger K, Zefferer M, Neufeld E, Rascher W, Janka R,  
51 Bautz W, Chen J, Kiefer B, Schmitt P, Hollenbach H-P, Shen J, Oberle M, Szczerba  
52 D, Kam A, Guag J W and Kuster N 2009 The Virtual Family—development of  
53 surface-based anatomical models of two adults and two children for dosimetric  
54 790 simulations *Phys. Med. Biol.* **55** N23-38  
55  
56  
57  
58 Constine L S, Ronckers C M, Hua C-H, Olch A, Kremer L C M, Jackson A and Bentzen S M  
59 2019 Pediatric Normal Tissue Effects in the Clinic (PENTEC): An International  
60

- 1  
2  
3 Collaboration to Analyse Normal Tissue Radiation Dose-Volume Response  
4 795 Relationships for Paediatric Cancer Patients *Clin. Oncol.* **31** 199-207  
5  
6  
7 Dickie D A, Shenkin S D, Anblagan D, Lee J, Blesa Cabez M, Rodriguez D, Boardman J P,  
8 Waldman A, Job D E and Wardlaw J M 2017 Whole Brain Magnetic Resonance  
9 Image Atlases: A Systematic Review of Existing Atlases and Caveats for Use in  
10 Population Imaging *Front. Neuroinformatics* **11** Online:  
11  
12 800 <https://www.ncbi.nlm.nih.gov/pmc/articles/PMC5244468/>  
13  
14  
15 Dréan G, Acosta O, Ospina J D, Fargeas A, Lafond C, Corrége G, Lagrange J-L, Créhange  
16 G, Simon A, Haigrón P and de Crevoisier R 2016 Identification of a rectal  
17 subregion highly predictive of rectal bleeding in prostate cancer IMRT *Radiother.*  
18 *Oncol.* **119** 388-97  
19  
20  
21  
22 805 Fonov V, Evans A C, Botteron K, Almli C R, McKinstry R C, Collins D L, and Brain  
23 Development Cooperative Group 2011 Unbiased average age-appropriate atlases  
24 for pediatric studies *NeuroImage* **54** 313-27  
25  
26  
27  
28 Ghosh S S, Kakunoori S, Augustinack J, Nieto-Castanon A, Kovelman I, Gaab N,  
29 Christodoulou J A, Triantafyllou C, Gabrieli J D E and Fischl B 2010 Evaluating the  
30 810 Validity of Volume-Based and Surface-Based Brain Image Registration for  
31 Developmental Cognitive Neuroscience Studies in Children 4-to-11 Years of Age  
32 *NeuroImage* **53** 85-93  
33  
34  
35  
36 Gunther J R, Sato M, Chintagumpala M, Ketonen L, Jones J Y, Allen P K, Paulino A C, Okcu  
37 M F, Su J M, Weinberg J, Boehling N S, Khatua S, Adesina A, Dauser R, Whitehead  
38 815 W E and Mahajan A 2015 Imaging Changes in Pediatric Intracranial Ependymoma  
39 Patients Treated With Proton Beam Radiation Therapy Compared to Intensity  
40 Modulated Radiation Therapy *Int. J. Radiat. Oncol. Biol. Phys.* **93** 54-63  
41  
42  
43  
44 Harrison R M 2013 Introduction to dosimetry and risk estimation of second cancer  
45 induction following radiotherapy *Radiat. Meas.* **57** 1-8  
46  
47  
48 820 Ibragimov B, Toesca D, Chang D, Yuan Y, Koong A and Xing L 2018 Development of deep  
49 neural network for individualized hepatobiliary toxicity prediction after liver SBRT  
50 *Med. Phys.* **45** 4763-74  
51  
52  
53 Ibragimov B, Toesca D, Yuan Y, Koong A, Daniel C and Xing L 2019 Neural networks for  
54 deep radiotherapy dose analysis and prediction of liver SBRT outcomes *IEEE J.*  
55 825 *Biomed. Health Inform.* 1-1  
56  
57  
58 Iglesias J E and Sabuncu M R 2015 Multi-Atlas Segmentation of Biomedical Images: A  
59 Survey *Med. Image Anal.* **24** 205-19  
60

- 1  
2  
3 Inskip P D, Robison L L, Stovall M, Smith S A, Hammond S, Mertens A C, Whitton J A, Diller  
4 L, Kenney L, Donaldson S S, Meadows A T and Neglia J P 2009 Radiation Dose and  
5 Breast Cancer Risk in the Childhood Cancer Survivor Study *J. Clin. Oncol.* **27** 3901-  
6 830 7  
7  
8  
9  
10 Johnson H J and Christensen G E 2002 Consistent landmark and intensity-based image  
11 registration *IEEE Trans. Med. Imaging* **21** 450-61  
12  
13  
14 Joshi S, Davis B, Jomier M and Gerig G 2004 Unbiased diffeomorphic atlas construction for  
15 835 computational anatomy *NeuroImage* **23** S151-60  
16  
17  
18 Lawell M P, Indelicato D J, Paulino A C, Hartsell W, Laack N N, Ermoian R P, Perentesis J P,  
19 Vatner R, Perkins S, Mangona V S, Hill-Kayser C E, Wolden S L, Kwok Y, Chang J H-  
20 C, Wilkinson J B, MacEwan I, Chang A L, Eaton B R, Ladra M M, Gallotto S L,  
21 Weyman E A, Bajaj B V M, Baliga S, Yeap B Y, Berrington de Gonzalez A and Yock  
22 840 T I 2019 An open invitation to join the Pediatric Proton/Photon Consortium  
23 Registry to standardize data collection in pediatric radiation oncology *Br. J. Radiol.*  
24 **93** 20190673  
25  
26  
27  
28  
29 Lee C, Jung J W, Pelletier C, Pyakuryal A, Lamart S, Kim J O and Lee C 2015  
30 Reconstruction of organ dose for external radiotherapy patients in retrospective  
31 845 epidemiologic studies *Phys. Med. Biol.* **60** 2309-24  
32  
33  
34 Lim P S, Rompokos V, Bizzocchi N, Gillies C, Gosling A, Royle G, Chang Y-C, Gaze M N and  
35 Gains J E 2020 Pencil Beam Scanning Proton Therapy Case Selection for Paediatric  
36 Abdominal Neuroblastoma: Effects of Tumour Location and Bowel Gas *Clin. Oncol.*  
37 **0** Online: [https://www.clinicaloncologyonline.net/article/S0936-6555\(20\)30361-](https://www.clinicaloncologyonline.net/article/S0936-6555(20)30361-7/abstract)  
38 850 [7/abstract](https://www.clinicaloncologyonline.net/article/S0936-6555(20)30361-7/abstract)  
39  
40  
41  
42 Ludmir E B, Grosshans D R and Woodhouse K D 2018 Radiotherapy Advances in Pediatric  
43 Neuro-Oncology *Bioeng. Basel Switz.* **5**  
44  
45  
46 Marcello M, Denham J W, Kennedy A, Haworth A, Steigler A, Greer P B, Holloway L C,  
47 Dowling J A, Jameson M G, Roach D, Joseph D J, Gulliford S L, Dearnaley D P, Sydes  
48 855 M R, Hall E and Ebert M A 2020 Reduced Dose Posterior to Prostate Correlates  
49 With Increased PSA Progression in Voxel-Based Analysis of 3 Randomized Phase 3  
50 Trials *Int. J. Radiat. Oncol.* **108** 1304-18  
51  
52  
53  
54 McWilliam A, Kennedy J, Hodgson C, Vasquez Osorio E, Faivre-Finn C and van Herk M  
55 2017 Radiation dose to heart base linked with poorer survival in lung cancer  
56 860 patients *Eur. J. Cancer* **85** 106-13  
57  
58  
59  
60

- 1  
2  
3 McWilliam A, Khalifa J, Vasquez Osorio E, Banfill K, Abravan A, Faivre-Finn C and van Herk  
4 M 2020 Novel Methodology to Investigate the Effect of Radiation Dose to Heart  
5 Substructures on Overall Survival *Int. J. Radiat. Oncol.* **108** 1073–81  
6  
7  
8  
9 Mesbah L, Matute R, Usyckin S, Marrone I, Puebla F, Mínguez C, García R, García G,  
10 865 Beltrán C and Marsiglia H 2011 Helical tomotherapy in the treatment of pediatric  
11 malignancies: a preliminary report of feasibility and acute toxicity *Radiat. Oncol.*  
12 *Lond. Engl.* **6** 102  
13  
14  
15 Mishchenko Y 2015 A fast algorithm for computation of discrete Euclidean distance  
16 transform in three or more dimensions on vector processing architectures *Signal*  
17 *Image Video Process.* **9** 19–27  
18 870  
19  
20  
21 Modat M, Cash D M, Daga P, Winston G P, Duncan J S and Ourselin S 2014 Global image  
22 registration using a symmetric block-matching approach *J. Med. Imaging* **1**  
23 024003  
24  
25  
26 Modat M, Daga P, Cardoso M J, Ourselin S, Ridgway G R and Ashburner J 2012 Parametric  
27 875 non-rigid registration using a stationary velocity field *2012 IEEE Workshop on*  
28 *Mathematical Methods in Biomedical Image Analysis* 2012 IEEE Workshop on  
29 Mathematical Methods in Biomedical Image Analysis pp 145–50  
30  
31  
32  
33 Monti S, Pacelli R, Cella L and Palma G 2018 Inter-patient image registration algorithms  
34 to disentangle regional dose bioeffects *Sci. Rep.* **8** 4915  
35  
36  
37 880 Monti S, Paganelli C, Buizza G, Preda L, Valvo F, Baroni G, Palma G and Cella L 2020 A  
38 novel framework for spatial normalization of dose distributions in voxel-based  
39 analyses of brain irradiation outcomes *Phys. Med.* **69** 164–9  
40  
41  
42 Monti S, Palma G, D'Avino V, Gerardi M, Marvaso G, Ciardo D, Pacelli R, Jereczek-Fossa B  
43 A, Alterio D and Cella L 2017 Voxel-based analysis unveils regional dose  
44 885 differences associated with radiation-induced morbidity in head and neck cancer  
45 patients *Sci. Rep.* **7** 7220  
46  
47  
48  
49 Mylona E, Acosta O, Lizee T, Lafond C, Crehange G, Magné N, Chiavassa S, Supiot S,  
50 Arango J D O, Campillo-Gimenez B, Castelli J and Crevoisier R de 2019 Voxel-  
51 Based Analysis for Identification of Urethrovesical Subregions Predicting Urinary  
52 890 Toxicity After Prostate Cancer Radiation Therapy *Int. J. Radiat. Oncol. Biol. Phys.*  
53 **104** 343–54  
54  
55  
56  
57 Mylona E, Ebert M, Kennedy A, Joseph D, Denham J, Steigler A, Supiot S, Acosta O and de  
58 Crevoisier R 2020 Rectal and Urethro-Vesical Subregions for Toxicity Prediction  
59  
60

- 1  
2  
3 After Prostate Cancer Radiation Therapy: Validation of Voxel-Based Models in an  
4 Independent Population *Int. J. Radiat. Oncol.* **108** 1189–95  
5 895
- 6  
7 Namburete A I L, van Kampen R, Papageorghiou A T and Papież B W 2018 Multi-channel  
8 Groupwise Registration to Construct an Ultrasound-Specific Fetal Brain Atlas *Data*  
9 *Driven Treatment Response Assessment and Preterm, Perinatal, and Paediatric*  
10 *Image Analysis* Lecture Notes in Computer Science ed A Melbourne, R Licandro, M  
11 DiFranco, P Rota, M Gau, M Kampel, R Aughwane, P Moeskops, E Schwartz, E  
12 900 Robinson and A Makropoulos (Cham: Springer International Publishing) pp 76–86  
13  
14  
15  
16  
17 Ourselin S, Roche A, Subsol G, Pennec X and Ayache N 2001 Reconstructing a 3D  
18 structure from serial histological sections *Image Vis. Comput.* **19** 25–31  
19  
20  
21 Padovani L, Horan G and Ajithkumar T 2019 Radiotherapy Advances in Paediatric  
22 905 Medulloblastoma Treatment *Clin. Oncol.* **31** 171–81  
23  
24  
25 Palma G, Monti S, Buonanno A, Pacelli R and Cella L 2019a PACE: A Probabilistic Atlas for  
26 Normal Tissue Complication Estimation in Radiation Oncology *Front. Oncol.* **9**  
27 Online: <https://www.frontiersin.org/articles/10.3389/fonc.2019.00130/full>  
28  
29  
30 Palma G, Monti S and Cella L 2020 Voxel-based analysis in radiation oncology: A  
31 910 methodological cookbook *Phys. Med.* **69** 192–204  
32  
33  
34 Palma G, Monti S, D'Avino V, Conson M, Liuzzi R, Pressello M C, Donato V, Deasy J O,  
35 Quarantelli M, Pacelli R and Cella L 2016 A Voxel-Based Approach to Explore Local  
36 Dose Differences Associated With Radiation-Induced Lung Damage *Int. J. Radiat.*  
37 *Oncol.* **96** 127–33  
38  
39  
40  
41 915 Palma G, Monti S, Thor M, Rimner A, Deasy J O and Cella L 2019b Spatial signature of  
42 dose patterns associated with acute radiation-induced lung damage in lung  
43 cancer patients treated with stereotactic body radiation therapy *Phys. Med. Biol.*  
44 **64** 155006  
45  
46  
47  
48 Pappo A S, Furman W L, Schultz K A, Ferrari A, Helman L and Krailo M D 2015 Rare  
49 920 Tumors in Children: Progress Through Collaboration *J. Clin. Oncol.* **33** 3047–54  
50  
51  
52 Paulino A C, Constine L S, Rubin P and Williams J P 2010 Normal Tissue Development,  
53 Homeostasis, Senescence, and the Sensitivity to Radiation Injury Across the Age  
54 Spectrum *Semin. Radiat. Oncol.* **20** 12–20  
55  
56  
57 Pilia M, Kullberg J, Ahlström H, Malmberg F, Ekström S and Strand R 2019 Average  
58 925 volume reference space for large scale registration of whole-body magnetic  
59 resonance images *PLOS ONE* **14** e0222700  
60

- 1  
2  
3 Rivest-Hénault D, Greer P, Fripp J and Dowling J 2014 Structure-Guided Nonrigid  
4 Registration of CT-MR Pelvis Scans with Large Deformations in MR-Based Image  
5 Guided Radiation Therapy *Clinical Image-Based Procedures. Translational*  
6 *Research in Medical Imaging Lecture Notes in Computer Science* ed M Erdt, M G  
7 930 Linguraru, C Oyarzun Laura, R Shekhar, S Wesarg, M A González Ballester and K  
8 Drechsler (Cham: Springer International Publishing) pp 65–73  
9  
10  
11  
12  
13 Roddy E and Mueller S 2016 Late Effects of Treatment of Pediatric Central Nervous  
14 System Tumors *J. Child Neurol.* **31** 237–54  
15  
16  
17 935 Rohlfing T, Brandt R, Menzel R and Maurer C R 2004 Evaluation of atlas selection  
18 strategies for atlas-based image segmentation with application to confocal  
19 microscopy images of bee brains *NeuroImage* **21** 1428–42  
20  
21  
22 Rueckert D, Sonoda L I, Hayes C, Hill D L G, Leach M O and Hawkes D J 1999 Nonrigid  
23 registration using free-form deformations: application to breast MR images *IEEE*  
24 940 *Trans. Med. Imaging* **18** 712–21  
25  
26  
27 Schneider U, Agosteo S, Pedroni E and Besserer J 2002 Secondary neutron dose during  
28 proton therapy using spot scanning *Int. J. Radiat. Oncol.* **53** 244–51  
29  
30  
31 Schneider U, Sumila M and Robotka J 2011 Site-specific dose-response relationships for  
32 cancer induction from the combined Japanese A-bomb and Hodgkin cohorts for  
33 doses relevant to radiotherapy *Theor. Biol. Med. Model.* **8** 27  
34 945  
35  
36  
37 Schwartz C L 1999 Long-Term Survivors of Childhood Cancer: The Late Effects of Therapy  
38 *The Oncologist* **4** 45–54  
39  
40  
41 Segars W P, Sturgeon G, Li X, Cheng L, Ceritoglu C, Ratnanather J T, Miller M I, Tsui B,  
42 Frush D and Samei E 2009 Patient specific computerized phantoms to estimate  
43 dose in pediatric CT *Progress in Biomedical Optics and Imaging - Proceedings of*  
44 950 *SPIE Medical Imaging 2009: Physics of Medical Imaging* p 72580H Online:  
45 [https://jhu.pure.elsevier.com/en/publications/patient-specific-computerized-](https://jhu.pure.elsevier.com/en/publications/patient-specific-computerized-phantoms-to-estimate-dose-in-pediat-3)  
46 [phantoms-to-estimate-dose-in-pediat-3](https://jhu.pure.elsevier.com/en/publications/patient-specific-computerized-phantoms-to-estimate-dose-in-pediat-3)  
47  
48  
49  
50 Skinner R 2018 Late renal toxicity of treatment for childhood malignancy: risk factors,  
51 955 long-term outcomes, and surveillance *Pediatr. Nephrol. Berl. Ger.* **33** 215–25  
52  
53  
54 Sterzing F, Stoiber E M, Nill S, Bauer H, Huber P, Debus J and Münter M W 2009 Intensity  
55 modulated radiotherapy (IMRT) in the treatment of children and Adolescents - a  
56 single institution's experience and a review of the literature *Radiat. Oncol. Lond.*  
57 *Engl.* **4** 37  
58  
59  
60

- 1  
2  
3 960 Strand R, Malmberg F, Johansson L, Lind L, Sundbom M, Ahlström H and Kullberg J 2017 A  
4 concept for holistic whole body MRI data analysis, *Imiomics PLOS ONE* **12**  
5 e0169966  
6  
7  
8 The Royal College of Radiologists 2019 *Radiotherapy dose fractionation* (Clinical  
9 Oncology) Online: [https://www.rcr.ac.uk/publication/radiotherapy-dose-](https://www.rcr.ac.uk/publication/radiotherapy-dose-fractionation-third-edition)  
10 [fractionation-third-edition](https://www.rcr.ac.uk/publication/radiotherapy-dose-fractionation-third-edition)  
11 965  
12  
13 Trott K-R 2017 Special radiobiological features of second cancer risk after particle  
14 radiotherapy *Phys. Medica PM Int. J. Devoted Appl. Phys. Med. Biol. Off. J. Ital.*  
15 *Assoc. Biomed. Phys. AIFB* **42** 221-7  
16  
17  
18  
19 Veiga C, Landau D, McClelland J R, Ledermann J A, Hawkes D, Janes S M and Devaraj A  
20 970 2018 Long term radiological features of radiation-induced lung damage *Radiother.*  
21 *Oncol.* **126** 300-6  
22  
23  
24  
25 Viselner G, Farina L, Lucev F, Turpini E, Lungarotti L, Bacila A, Iannalfi A, D'Ippolito E,  
26 Vischioni B, Ronchi S, Marchioni E, Valvo F, Bastianello S and Preda L 2019 Brain  
27 MR findings in patients treated with particle therapy for skull base tumors *Insights*  
28 975 *Imaging* **10** 94  
29  
30  
31 Wang Q, Chen L, Yap P-T, Wu G and Shen D 2010 Groupwise registration based on  
32 hierarchical image clustering and atlas synthesis *Hum. Brain Mapp.* **31** 1128-40  
33  
34  
35 Xie T, Kuster N and Zaidi H 2017 Computational hybrid anthropometric paediatric  
36 phantom library for internal radiation dosimetry *Phys. Med. Biol.* **62** 3263-83  
37  
38  
39 980 Xu X G, Bednarz B and Paganetti H 2008 A review of dosimetry studies on external-beam  
40 radiation treatment with respect to second cancer induction *Phys. Med. Biol.* **53**  
41 R193-241  
42  
43  
44 Yankeelov T E, Abramson R G and Quarles C C 2014 Quantitative multimodality imaging  
45 in cancer research and therapy *Nat. Rev. Clin. Oncol.* **11** 670-80  
46  
47  
48 985 Yushkevich P A, Piven J, Hazlett H C, Smith R G, Ho S, Gee J C and Gerig G 2006 User-  
49 guided 3D active contour segmentation of anatomical structures: significantly  
50 improved efficiency and reliability *NeuroImage* **31** 1116-28  
51  
52  
53 Zhou L, Salvado O, Dore V, Bourgeat P, Raniga P, Macaulay S L, Ames D, Masters C L,  
54 Ellis K A, Villemagne V L, Rowe C C, Frapp J and Group A R 2014 MR-Less Surface-  
55 Based Amyloid Assessment Based on 11C PiB PET *PLOS ONE* **9** e84777  
56 990  
57  
58  
59  
60